Int J Adv Manuf Technol (2017) 89:2845–2862
DOI 10.1007/s00170-016-9830-7

ORIGINAL ARTICLE

Regenerative chatter in a plunge grinding process with workpiece imbalance

Yao Yan[1] · Jian Xu[2] · Marian Wiercigroch[3]

Received: 23 July 2016 / Accepted: 24 November 2016 / Published online: 20 December 2016

Abstract Grinding vibrations caused by regenerative cutting force and workpiece imbalance are discussed in this study. To regenerate workpiece surface, a grinding wheel is rotated, and pushed towards a rotating workpiece, rubbing and cutting its surface, with regenerative and frictional interactive forces generated. Besides, any mass imbalances of the rotating workpiece or the wheel is another source of vibration. To investigate both effects of the regeneration and the mass eccentricity on the grinding dynamics, a mathematical model with time delays and sinusoid excitation has been developed and analysed. By calculating eigenvalues with continuation scheme, linearly grinding stability is obtained and presented in a *lobes* diagram, where chatter-free and chatter regions are identified. For chatter without workpiece imbalance, a classical periodic chatter induced by the regenerative effect is found. With imbalance, forced periodic vibration, chatter quenching, quasi-periodic chatter and periodic chatter are obtained in different regions.

Keywords Regenerative grinding chatter · Workpiece imbalance · State-dependent time delay · Coulomb friction · Chatter quenching

✉ Jian Xu
xujian@tongji.edu.cn

Yao Yan
y.yan@uestc.edu.cn

Marian Wiercigroch
m.wiercigroch@abdn.ac.uk

[1] School of Aeronautics and Astronautics, University of Electronic Science and Technology of China, Chengdu 611731, China

[2] School of Aerospace Engineering and Applied Mechanics, Tongji University, Shanghai 200092, China

[3] Centre for Applied Dynamics Research, School of Engineering, Fraser Noble Building, King's College, University of Aberdeen, Aberdeen, AB24 3UE Scotland, UK

1 Introduction

In majority of machining operations the surface product quality depends on grinding process which in turn relies on process stability, since unstable grinding introduces vibration, which compromises geometrical accuracy and surface finishing, and also reduces a tool life [1, 26]. Therefore, it is crucial to understand the mechanisms of grinding vibration in order to suppress them effectively [14]. In general, grinding instability can be externally introduced or self-induced. The sources of forced vibration include imbalances of wheel, rotary dresser, spindle, motor and pulley wheel [34]. On the other hand, the self-excited machining vibration can be classified as frictional, regenerative, model-coupling and thermo-mechanical [43].

Among various self-excited grinding vibrations, the regenerative chatter is the most dangerous and has attracted more attention than any other types of chatter. In 1954, when the regenerative theory for turning processes was developed by Arnold, the regenerative stability of an internal-grinding process with a wear-resistant wheel was first discussed by Hahn using the Nyquist criteria [2, 10]. Then, a similar analysis was performed by Snoeys and Brown to investigate stability of a cylindrical grinding process with a wheel wear [35]. Later on, an alternative approach for the analysis of the grinding stability was proposed by Thompson [39, 40]. Using his kinematic model, the Laplace transform

as well as the exponential growth index, Thompson successively studied various effects on grinding stability including contact stiffness and wave filtering [37, 38, 41]. Thereafter, Yuan et al. [48] proposed a nonlinear kinetic model to describe the double regenerative grinding. This model was then linearised by Liu and Payre [24], who proposed a novel numerical algorithm to study grinding stability. Then, nonlinearity in the grinding force was considered by Chung and Liu [5], who used a perturbation scheme to study the grinding chatter induced by supercritical Hopf bifurcation. Thereafter, the Bautin bifurcation induced chatter in both plunge and traverse grinding processes was investigated by Yan et al. and Kim et al., respectively [19, 20, 45].

Besides the self-excited regenerative vibration, another major source of instability is rotating spindle imbalance, i.e. a workpiece imbalance in grinding. This is due to a mismatch between the axis of the moment of inertia of the spindle and its axis of rotation [31], and its corresponding vibration is associated with so-called rotor dynamics. For a rotating spindle, this vibration can be attributed an imbalance caused by many effects including accumulation of dirt, corrosion, erosion and rotor-bearing interaction and others [33, 49]. The dynamics of rotary shafts was first modelled and systematically studied by Jeffcott, and thus such a model is coined as "Jeffcott rotor" [16]. Thereafter, a numerous studies have been performed to analyses this model. For example, Diken [8] investigated sub-harmonic whirling in a slender Jeffcott rotor. Various dynamical motions of a Jeffcott rotor with snubber ring were analysed by Karpenko et al. [17, 18] and Páez Chávez and Wiercigroch [30]. Torsional vibration of a Jeffcott rotor was studied by Vlajic et al. [42]. Bifurcation analyses of a nonlinear buckled Jeffcott rotor system were carried out by Huang et al. [11, 12]. Effects of a water-film whirl and whip on the rotor dynamics were discussed by Zhai et al. [49]. Simply put, the rotor dynamics has received a significant attention investigation since it is very crucial for rotating spindles.

In machining processes, rotating components are comprehensively used, and thus rotor dynamics of a spindle with eccentricity should be considered. To illustrate this point, in the analysis of turning dynamics, vibration with a workpiece imbalance were studied by Dassanayake et al. [6, 7], who numerically modelled whirling vibration of the spindle with three discs. Huang et al. [13] investigated the turning dynamics influenced by an imbalance of aerostatic bearing spindle, and they observed significant changes of vibration amplitude for different spindle speeds. Tauhiduzzaman et al. [36] regarded the rotor vibration due to a spindle imbalance as the major cause of machining error in a diamond turning process. Inazaki and Yonetsu theoretically and experimentally investigated the effects of wheel imbalance and eccentricity on the amplitude of workpiece waves in a surface grinding process [15]. Given both forced vibration and self-excited regenerative chatter, the mass eccentricity of the grinding wheel and its effect on grinding force and workpiece waviness were first investigated by Badger et al. [3]. The dynamics of a robotic grinding process with mass eccentricity was experimentally analysed by Rafieian et al. [32], and a cyclic-impact grinding vibration was observed. Up to now, however, there has been no research on the regenerative grinding chatter combined with the effect of the rotor dynamics.

For the analysis of the grinding chatter with a mass imbalance in the workpiece, the rest of this paper is organized as follows. A dynamic model of the plunge grinding process is proposed in Section 2, where the vertical and horizontal workpiece movements, and horizontal wheel motion are all considered. The regenerative and frictional effects between the wheel and the workpiece are modelled. Also, the workpiece mass eccentricity is included resulting in an additional harmonic excitation. Then, this model is linearised in Section 3 to calculate eigenvalues for the stability analysis. In Section 4, numerical simulation and bifurcation analysis are used to investigate stability and various grinding vibrations. Lastly, some relevant conclusions are drawn in Section 5.

2 Description of the plunge grinding

In a cylindrical grinding process, a rotary wheel is plunged into a workpiece in its radial direction, cutting and regenerating its surface with grits. Meanwhile, the workpiece is rotated by a chuck, feeding the wheel in its circumferential direction. As the workpiece is successively rubbed away by the wheel, a grinding force between the wheel and the workpiece is generated pushing each other away. According to the regenerative chatter theory [2, 24], it is known that the grinding force is proportional to the instantaneous grinding depth [9]. Any fluctuation in the depth induces variation of the force, and consequently the time-varying force excites the wheel and the workpiece to vibrate. Then, the change of wheel and workpiece displacements fluctuates the grinding depth and the force. This self-excited vibration, which is called regenerative chatter, is maintained as long as the system damping is insufficient.

In addition, due to the rotation of the wheel and the workpiece, any mass imbalance in the rotors can create another instability source for the grinding [31]. For rotating machinery, moreover, a mass imbalance can be the main cause of the vibration. Correspondingly, the rotor undergoes an externally forced periodic vibration.

Thus, to understand the grinding dynamics involving both the regenerative effect and the workpiece imbalance, a mathematical model based on the regenerative theory and the rotor dynamics is to be proposed.

2.1 Mathematical modelling of the grinding process

A schematic of the plunge grinding is depicted in Fig. 1, where the workpiece at its left end ($S = L$) is simply-supported by a tailstock and its right end ($S = 0$) is clamped and rotated by a chuck. The workpiece is of length L [m], radius R_w [m], Young's modulus E [Mp] and mass density ρ [kg m^{-3}]. Its damping coefficient is denoted as c_w [N s m^{-1}] and its rotation velocity as Ω_w [rad s^{-1}]. At $S = P$, a disc of the workpiece is cut which has width W [m] and radius r_p [m]. In addition, the mass distribution of the disc is not uniform resulting in a mass eccentricity $\mathbf{e}$ [m]. Due to the workpiece rotation, time evolution of the eccentricity is given by $\mathbf{e} = (e\sin(\Omega_\mathrm{w}t), e\cos(\Omega_\mathrm{w}t))^\mathrm{T}$. A grinding wheel is mounted on a wheel holder, which moves along a slot with feeding f [m] per workpiece revolution. The wheel is of mass m_g [kg] and radius R_g [m], stiffness k_g [N m^{-1}], damping coefficient c_g [N s m^{-1}] and rotates with angular velocity Ω_w [rad s^{-1}].

The workpiece shown in Fig. 1 can bend horizontally ($X_\mathrm{w}(t, S)$ [m]) and vertically ($Y_\mathrm{w}(t, S)$ [m]), while the wheel moves only in the direction of X_g [m]. Due to the vertical motion of the workpiece $Y_\mathrm{w}(t, S)$, there is a contact angle γ of the wheel-workpiece interaction. It is deducted from Fig. 2 that

$$\gamma = \tan^{-1}\left(\frac{a}{b}\right) = \tan^{-1}\left(\frac{Y_\mathrm{w}(t,\,P)}{R_\mathrm{g} + R_\mathrm{p} - f - X_\mathrm{w}(t,\,P) + X_\mathrm{g}(t)}\right). \quad (1)$$

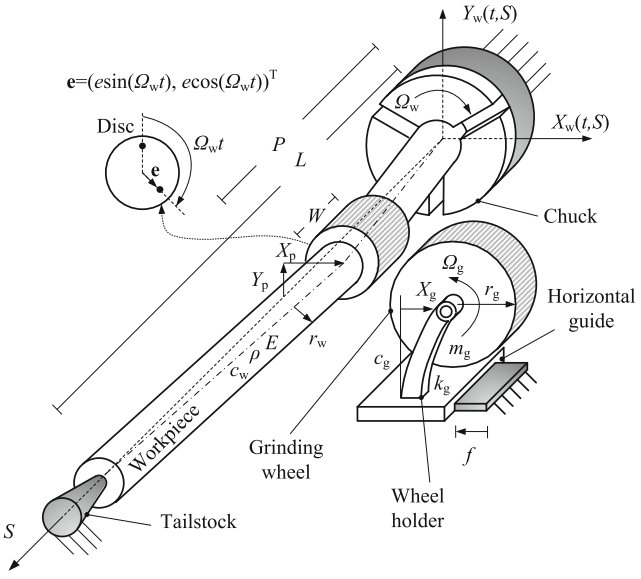

Fig. 1 Schematic of a plunge grinding process. A grinding wheel is mounted on a wheel holder, rotated and plunged into a workpiece. The workpiece is turned by a chuck, feeding the wheel to grind its disc located at $S = P$, which has a mass eccentricity $\mathbf{e}$

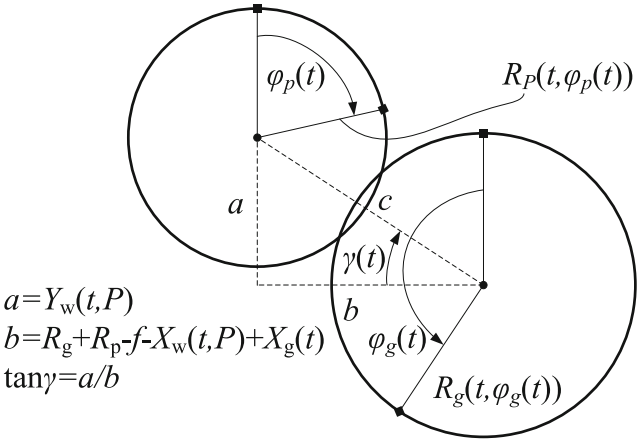

Fig. 2 Geometry of the wheel-workpiece interaction where the contact angle depends on the relative wheel-workpiece movement

The workpiece can be modelled as a spatial-temporal continuum beam with one end clamped and another simply-supported. As derived in Appendix A, the governing equation of the grinding dynamics is discretized to be [23]

$$\begin{aligned}
m_\mathrm{g}\frac{\mathrm{d}^2X_\mathrm{g}(t)}{\mathrm{d}t^2} + c_\mathrm{g}\frac{\mathrm{d}X_\mathrm{g}(t)}{\mathrm{d}t} + k_\mathrm{g}X_\mathrm{g}(t) &= F_x(t),\\
m_\mathrm{w}\frac{\mathrm{d}^2X_\mathrm{p}(t)}{\mathrm{d}t^2} + c_\mathrm{w}\frac{\mathrm{d}X_\mathrm{p}(t)}{\mathrm{d}t} + k_\mathrm{w}X_\mathrm{p}(t) &= 2em_\mathrm{d}\Omega_\mathrm{w}^2\sin(\Omega_\mathrm{w}t) - F_x(t),\\
m_\mathrm{w}\frac{\mathrm{d}^2Y_\mathrm{p}(t)}{\mathrm{d}t^2} + c_\mathrm{w}\frac{\mathrm{d}Y_\mathrm{p}(t)}{\mathrm{d}t} + k_\mathrm{w}Y_\mathrm{p}(t) &= 2em_\mathrm{d}\Omega_\mathrm{w}^2\cos(\Omega_\mathrm{w}t) + F_y(t),
\end{aligned} \quad (2)$$

where m_w [kg] and k_w [N m^{-1}] are the equivalent workpiece mass and stiffness estimated in Appendix A. Moreover, it should be noticed here that the terms, $2em_\mathrm{d}\Omega_\mathrm{w}^2\sin(\Omega_\mathrm{w}t)$ and $2em_\mathrm{d}\Omega_\mathrm{w}^2\cos(\Omega_\mathrm{w}t)$, stand for the effect of the mass imbalance, which exert sinusoid excitation on the workpiece in the directions of X and Y.

2.2 Grinding force

Besides the imbalance excitation, another instability source for Eq. 2 lies in $F_x(t)$ and $F_y(t)$, the interaction grinding forces [26]. As depicted in Fig. 3, $F_x(t)$ and $F_y(t)$ are X- and Y-components of the grinding force:

$$\begin{aligned}
F_x &= F_\mathrm{n}\cos\gamma + F_\mathrm{t}\sin\gamma,\\
F_y &= F_\mathrm{n}\sin\gamma - F_\mathrm{t}\cos\gamma,
\end{aligned} \quad (3)$$

where F_n [N] and F_t [N] represent normal and tangential grinding forces, respectively.

As an abrasive cutting tool, the grinding wheel uses small grinding particles to grind the workpiece, exerting interactive grinding force on the machining structure [26]. As seen in Fig. 4, each grinding particle of the wheel cuts and

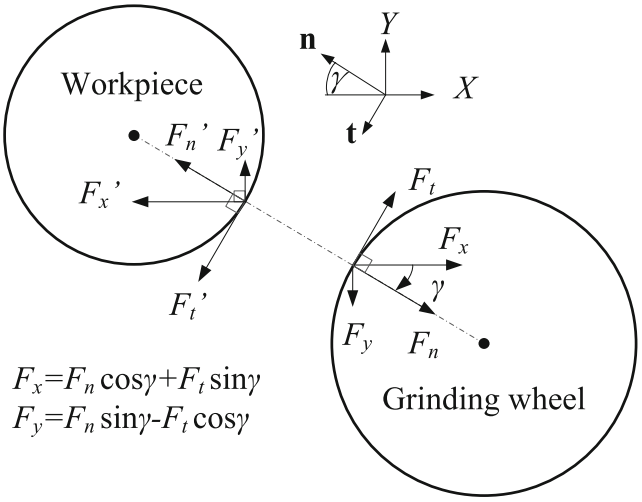

Fig. 3 Wheel-workpiece interaction force diagram in the plane

rubs the workpiece surface, generating cutting and frictional forces in the normal and tangential directions [9, 22]:

$$\begin{aligned} f_{\mathrm{ct}} &= \psi f_{\mathrm{cn}}, \\ f_{\mathrm{ft}} &= \mu f_{\mathrm{fn}}, \end{aligned} \tag{4}$$

where f_{ct} [N] and f_{cn} [N] are tangential and normal cutting forces, and f_{ft} [N] and f_{fn} [N] are tangential and normal frictional forces, respectively. Here, ψ is a dimensionless ratio depends on average tip angles of the grinding particles, and μ is a frictional coefficient.

Considering all grinding particles engages in the process, the total normal and tangential grinding forces can be expressed as [9]

$$\begin{aligned} F_{\mathrm{n}} &= WK_{\mathrm{c}}\frac{\Omega_{\mathrm{w}}}{\Omega_{\mathrm{g}}}D_{\mathrm{g}}(t) + WK_{\mathrm{f}}\frac{\Omega_{\mathrm{w}}}{\Omega_{\mathrm{g}}}D_{\mathrm{g}}(t)^{\frac{1}{2}}, \\ F_{\mathrm{t}} &= \psi WK_{\mathrm{c}}\frac{\Omega_{\mathrm{w}}}{\Omega_{\mathrm{g}}}D_{\mathrm{g}}(t) + \mu WK_{\mathrm{f}}\frac{\Omega_{\mathrm{w}}}{\Omega_{\mathrm{g}}}D_{\mathrm{g}}(t)^{\frac{1}{2}}, \end{aligned} \tag{5}$$

where K_{c} [N m^{-2}] and K_{f} [N m$^{-\frac{3}{2}}$] are the process coefficients for the cutting and the friction, respectively. Here, $D_{\mathrm{g}}(t)$ is instantaneous grinding depth depending on the feed and the relative wheel-workpiece displacements.

The grinding depth $D_{\mathrm{g}}(t)$ can be formulated according to the regenerative theory. The feed f makes a nominal depth $D_{\mathrm{n}} = f$ [m] when disregarding the relative wheel-workpiece displacement. When this displacement is included, the depth becomes

$$D_{\mathrm{g}} = f\cos(\gamma(t)) + \left(X_{\mathrm{p}}(t)\cos(\gamma(t)) - X_{\mathrm{g}}(t)\cos(\gamma(t)) - Y_{\mathrm{p}}(t)\sin(\gamma)\right). \tag{6}$$

Moreover, as seen from Fig. 5, as workpiece material is successively removed by the wheel, a new surface is regenerated. As the result, any fluctuation of the relative wheel-workpiece displacement in the previous workpiece revolution (at time $t - T_{\mathrm{w}}$) influences $D_{\mathrm{g}}(t)$ as well. Correspondingly, $D_{\mathrm{g}}(t)$ can be re-written as

$$\begin{aligned} D_{\mathrm{g}} = {} & f\cos(\gamma(t)) + \left(X_{\mathrm{p}}(t)\cos(\gamma(t)) - X_{\mathrm{g}}(t)\cos(\gamma(t)) - Y_{\mathrm{p}}(t)\sin(\gamma(t))\right) \\ & -\left(X_{\mathrm{p}}(t-T_{\mathrm{w}})\cos(\gamma(t-T_{\mathrm{w}})) - X_{\mathrm{g}}(t-T_{\mathrm{w}})\cos(\gamma(t-T_{\mathrm{w}}))\right. \\ & \left.-Y_{\mathrm{p}}(t-T_{\mathrm{w}})\sin(\gamma(t-T_{\mathrm{w}}))\right). \end{aligned} \tag{7}$$

Furthermore, the wheel is wearing as it grinds the workpiece, hence this double regenerative effect results the depth to be

$$\begin{aligned} D_{\mathrm{g}} = {} & f\cos(\gamma(t)) + \left(X_{\mathrm{p}}(t)\cos(\gamma(t)) - X_{\mathrm{g}}(t)\cos(\gamma(t)) - Y_{\mathrm{p}}(t)\sin(\gamma(t))\right) \\ & -\left(X_{\mathrm{p}}(t-T_{\mathrm{w}})\cos(\gamma(t-T_{\mathrm{w}})) - X_{\mathrm{g}}(t-T_{\mathrm{w}})\cos(\gamma(t-T_{\mathrm{w}}))\right. \\ & \left.-Y_{\mathrm{p}}(t-T_{\mathrm{w}})\sin(\gamma(t-T_{\mathrm{w}}))\right) \\ & -g\left(X_{\mathrm{p}}(t-T_{\mathrm{g}})\cos(\gamma(t-T_{\mathrm{g}})) - X_{\mathrm{g}}(t-T_{\mathrm{g}})\cos(\gamma(t-T_{\mathrm{g}}))\right. \\ & \left.-Y_{\mathrm{p}}(t-T_{\mathrm{g}})\sin(\gamma(t-T_{\mathrm{g}}))\right), \end{aligned} \tag{8}$$

where g is a small dimensionless ratio, indicating that the wearing speed of the wheel is much slower than the regenerating speed of the workpiece [34].

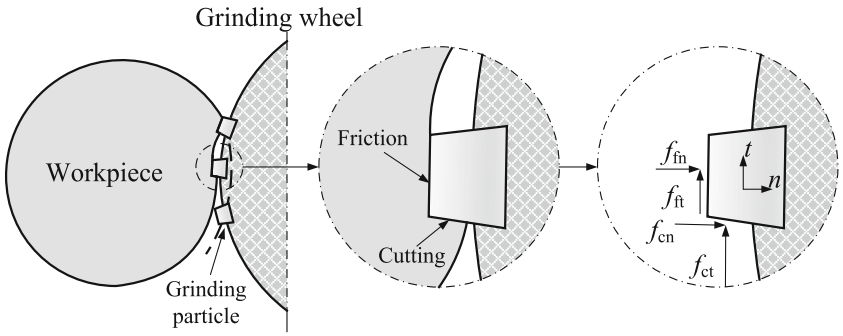

Fig. 4 Cutting and frictional forces generated by a single grinding particle

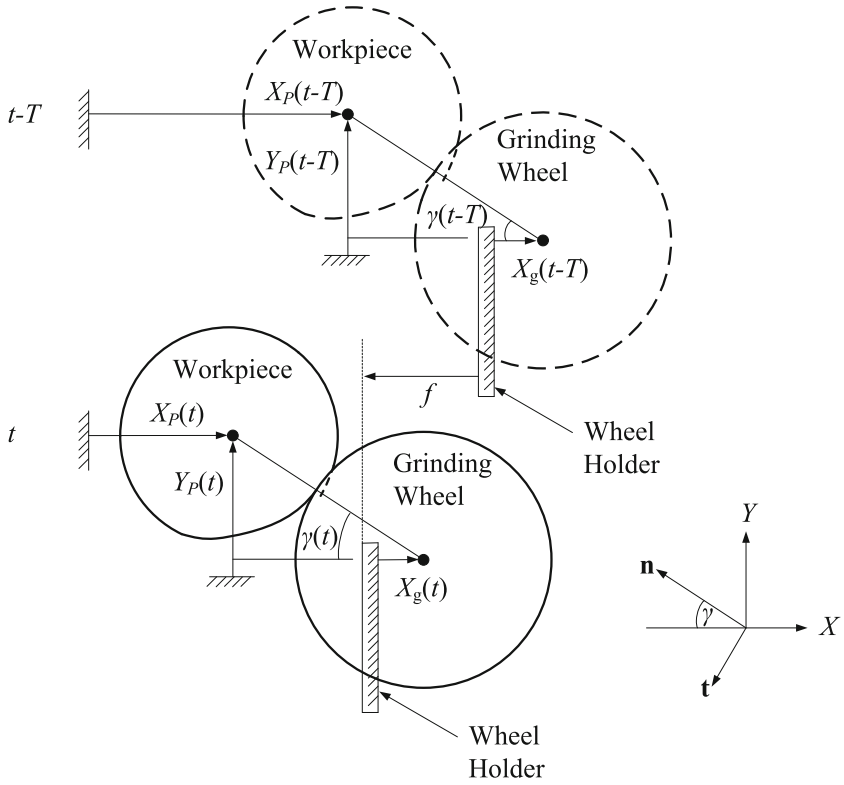

Fig. 5 A schematic of the regenerative grinding depth which depends on not only the current (t) wheel-workpiece displacement but also that in the previous revolution ($t - T$)

In case of no vertical workpiece motion, the rotation periods in Eq. 8, T_w and T_g are constant [24, 45]. However, if the contact angle γ is introduced by $Y_p(t)$, T_w and T_g, are transformed into the following state-dependent equations

$$\begin{aligned} 2\pi &= -\gamma(t) + \gamma(t - T_w) + T_w\Omega_w, \\ 2\pi &= \gamma(t) - \gamma(t - T_g) + T_g\Omega_g. \end{aligned} \tag{9}$$

Besides the regenerative effect, the friction is considered with a simple Coulomb model, where the frictional coefficient μ in Eq. 5 is modelled as

$$\mu = \text{sign}(V_f)\mu_d. \tag{10}$$

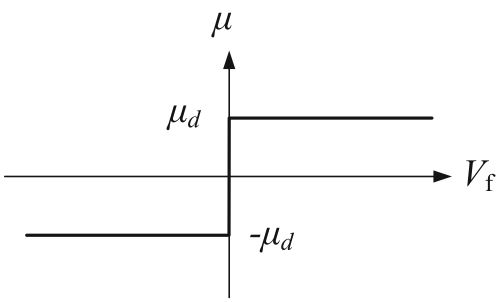

Fig. 6 Friction coefficient between the wheel and the workpiece as the function of the relative velocity V_f represented by a simple Coulomb model

It is shown in Fig. 6 that μ is a function of the tangential relative wheel-workpiece velocity V_f. As seen in Fig. 7, V_f depends on the wheel and workpiece rotations, as well as their planar motions, which is

$$V_f = V_{fg} - V_{fw}, \tag{11}$$

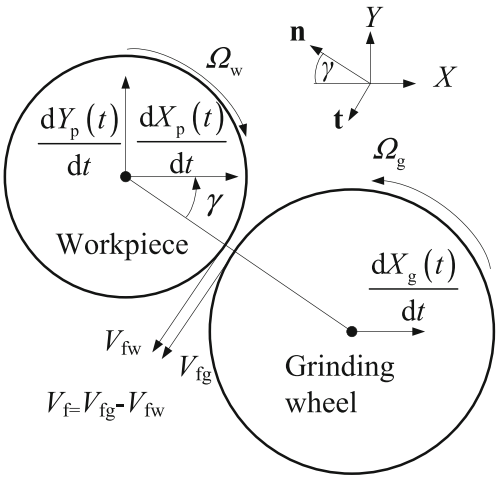

Fig. 7 Schematic showing tangential relative velocity between the wheel and the workpiece

Table 1 Parameter values converted from ref. [21]

Parameters	Symbols	Values
Workpiece mass [kg]	m_w	1.415
Workpiece damping [[N s m^{-1}]	c_w	247.126
Workpiece stiffness [N m^{-1}]	k_w	4.316×10^6
Workpiece radius [m]	R_p	0.0381
Wheel radius [m]	R_g	0.0889
Grinding width [m]	W	0.0127
Dimensionless ratio [-]	ψ	0.443
Frictional coefficient [-]	μ_d	0.443
Wheel period [s]	T_g	0.0177

where V_{fg} and V_{fw} are tangential velocities of the wheel and the workpiece at the contact zone:

$$\begin{aligned} V_{fg} &= \Omega_g R_g - \frac{dX_g(t)}{dt}\sin(\gamma), \\ V_{fw} &= \Omega_w R_p - \frac{dY_p(t)}{dt}\cos(\gamma) - \frac{dX_p(t)}{dt}\sin(\gamma). \end{aligned} \tag{12}$$

2.3 Dimensionless mathematical model of the grinding process with the workpiece imbalance

In order to undertake the stability analysis which results are generic, Eq. 2 is nondimensionalized by introducing the following dimensionless parameters:

$$\begin{gathered} \xi_g = \frac{c_g\sqrt{m_w}}{m_g\sqrt{k_w}}, \quad \xi_w = \frac{c_w\sqrt{m_w}}{m_w\sqrt{k_w}}, \\ \kappa_c = \frac{K_c m_w}{k_w m_g}(R_g + R_p), \quad \kappa_f = \frac{K_f m_w}{k_w m_g}\sqrt{R_g + R_p}, \quad \kappa_g = \frac{k_g m_w}{k_w m_g}, \\ \gamma_w = \frac{m_w}{m_g}, \quad \nu = \frac{f}{R_p + R_g}, \quad \delta = \frac{8e\pi^2 m_d}{m_w(R_p + R_g)} \\ r_p = \frac{R_p}{R_p + R_g}, \quad r_g = \frac{R_g}{R_p + R_g}, \quad p = \frac{P}{L}, \\ \omega_w = \Omega_w\sqrt{\frac{m_w}{k_w}}, \quad \omega_g = \Omega_g\sqrt{\frac{m_w}{k_w}}, \end{gathered} \tag{13}$$

and variables:

$$\begin{aligned} \tau &= t\sqrt{\tfrac{k_w}{m_w}}, \quad \tau_w = T_w\sqrt{\tfrac{k_w}{m_w}}, \quad \tau_g = T_g\sqrt{\tfrac{k_w}{m_w}}, \\ x_g(\tau) &= \tfrac{X_g(t)}{R_g+R_p}, \quad x_w(\tau) = \tfrac{X_w(t)}{R_g+R_p}, \quad y_w(\tau) = \tfrac{Y_w(t)}{R_g+R_p}, \\ \gamma &= \tan^{-1}\left(\tfrac{y_p(\tau)}{1-\nu-x_p(\tau)+x_g(\tau)}\right), \\ d_g &= \Big(\nu + x_p(\tau) - x_g(\tau)\Big)\cos(\gamma(\tau)) - y_p(t)\sin(\gamma(t)) \\ &\quad -\big(x_p(\tau-\tau_w) - x_g(\tau-\tau_w)\big)\cos(\gamma(\tau-\tau_w)) \\ &\quad +y_p(\tau-\tau_w)\sin(\gamma(\tau-\tau_w)) \\ &\quad -g\big(x_p(\tau-\tau_g) - x_g(\tau-\tau_g)\big)\cos(\gamma(\tau-\tau_g)) \\ &\quad +g y_p(\tau-\tau_g)\sin(\gamma(\tau-\tau_g)) \\ v_f &= \omega_g r_g - \omega_w r_p + \tfrac{dy_p(\tau)}{d\tau}\cos(\gamma) - \left(\tfrac{dx_g(\tau)}{d\tau} - \tfrac{dx_p(\tau)}{d\tau}\right)\sin(\gamma). \end{aligned} \tag{14}$$

As a result, the mathematical model of this grinding process expressed by Eq. 2 is transformed into

$$\begin{aligned} \frac{d^2x_g(\tau)}{d\tau^2} + \xi_g\frac{dx_g(\tau)}{d\tau} + \kappa_g x_g(\tau) = {} & w\kappa_f\frac{\tau_g}{\tau_w}\sqrt{d_g}\,(\cos(\gamma) + \mu\sin(\gamma)) \\ & + w\kappa_c\frac{\tau_g}{\tau_w}d_g\,(\cos(\gamma) + \psi\sin(\gamma)), \\ \frac{d^2x_p(\tau)}{d\tau^2} + \xi_w\frac{dx_p(\tau)}{d\tau} + x_p(\tau) = {} & -\frac{w\kappa_f}{\gamma_w}\frac{\tau_g}{\tau_w}\sqrt{d_g}\,(\cos(\gamma) + \mu\sin(\gamma)) \\ & -\frac{w\kappa_c}{\gamma_w}\frac{\tau_g}{\tau_w}d_g\,(\cos(\gamma) + \psi\sin(\gamma)) \\ & +\frac{\delta}{\tau_{w0}^2}\sin\left(\frac{2\pi}{\tau_{w0}}\tau\right), \\ \frac{d^2y_p(\tau)}{d\tau^2} + \xi_w\frac{dy_p(\tau)}{d\tau} + y_p(\tau) = {} & \frac{w\kappa_f}{\gamma_w}\frac{\tau_g}{\tau_w}\sqrt{d_g}\,(\sin(\gamma) - \mu\cos(\gamma)) \\ & +\frac{w\kappa_c}{\gamma_w}\frac{\tau_g}{\tau_w}d_g\,(\sin(\gamma) - \psi\cos(\gamma)) \\ & +\frac{\delta}{\tau_{w0}^2}\cos\left(\frac{2\pi}{\tau_{w0}}\tau\right). \end{aligned} \tag{15}$$

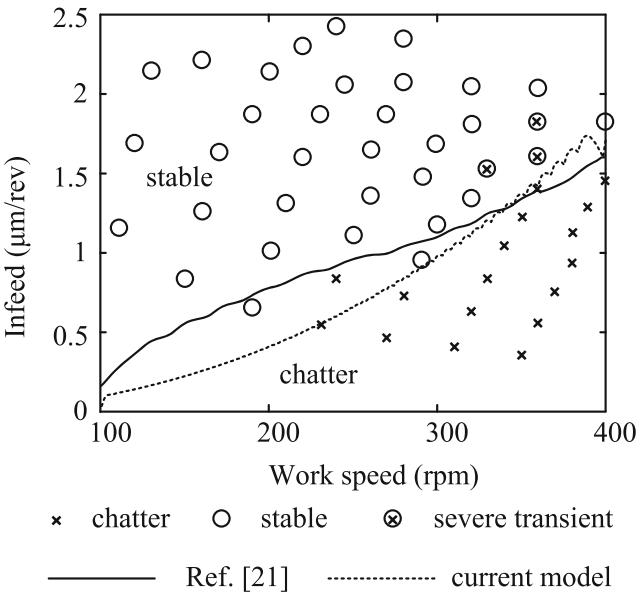

Fig. 8 Chatter boundaries obtained experimentally and theoretically, where the *solid and dashed lines* represent the boundaries predicted in ref. [21] and by the current model. *Circles and crosses* are marked for stable and unstable grinding processes observed in experiments [21]

2.4 Validation of the model

To validate the proposed model, a stability analysis is carried out, with its results compared with the experimental works performed by Li and Shin [21]. To this end, parameter values used in ref. [21] are converted for equivalent parameters in the new model, which are listed in Table 1. In addition, the coefficients for the regenerative and frictional grinding forces are selected as $K_c = 3.74 \times 10^7\ \mathrm{N\,m^{-2}}$, $K_c = 7.99 \times 10^5\ \mathrm{N\,m^{-\frac{3}{2}}}$ and $g = 0.1$. Employing the proposed model, ignoring the motion of the wheel and using the given parameter values, grinding stability is studied with eigenvalue analysis, yielding the stability boundary depicted in Fig. 8. It is seen that our model has a good performance in the prediction of the grinding stability, where the stable and unstable cases are divided by the dashed line. More details of the stability analysis with the new model are to be given in the next section.

3 Grinding stability analysis without the imbalance effect

We will gradually increase complexity when investigating the grinding stability of the considered model by first assuming zero eccentricity ($\delta = 0$), so that one can get some insight into mechanisms governing the grinding stability and the self-induced chatter.

3.1 Stable grinding

For the stability analysis, the state of steady grinding, namely the equilibrium of Eq. 15, must be known first. Hence, the constant displacements, $x_g(\tau) \equiv x_{g0}$, $x_p(\tau) \equiv x_{p0}$, and $y_p(\tau) \equiv y_{p0}$, and zero workpiece imbalance, $\delta = 0$, are substituted into Eq. 15, which leads to

$$\begin{aligned}
\kappa_g x_{g0} =\ & w\kappa_f \tfrac{\tau_{g0}}{\tau_{w0}} \sqrt{d_{g0}}\,(\cos(\gamma_0) + \mu \sin(\gamma_0)) \\
& + w\kappa_c \tfrac{\tau_{g0}}{\tau_{w0}} d_{g0}\,(\cos(\gamma_0) + \psi \sin(\gamma_0))\,, \\
x_{p0} =\ & -\tfrac{w\kappa_f}{\gamma_w} \tfrac{\tau_{g0}}{\tau_{w0}} \sqrt{d_{g0}}\,(\cos(\gamma_0) + \mu \sin(\gamma_0)) \\
& - \tfrac{w\kappa_c}{\gamma_w} \tfrac{\tau_{g0}}{\tau_{w0}} d_{g0}\,(\cos(\gamma_0) + \psi \sin(\gamma_0))\,, \\
y_{p0} =\ & \tfrac{w\kappa_f}{\gamma_w} \tfrac{\tau_{g0}}{\tau_{w0}} \sqrt{d_{g0}}\,(\sin(\gamma_0) - \mu \cos(\gamma_0)) \\
& + \tfrac{w\kappa_c}{\gamma_w} \tfrac{\tau_{g0}}{\tau_{w0}} d_{g0}\,(\sin(\gamma_0) - \psi \cos(\gamma_0))\,,
\end{aligned} \tag{16}$$

where

$$\begin{aligned}
\gamma_0 =\ & \tan^{-1}\left(\tfrac{y_{p0}}{1-\nu-x_{p0}+x_{g0}}\right), \\
d_{g0} =\ & \nu - g\left(x_{p0} - x_{g0}\right)\cos(\gamma_0) + g y_{p0} \sin(\gamma_0), \\
v_{f0} =\ & \omega_g r_g - \omega_w r_p, \\
\tau_{w0} =\ & \tfrac{2\pi}{\omega_w}, \\
\tau_{g0} =\ & \tfrac{2\pi}{\omega_g}.
\end{aligned} \tag{17}$$

3.2 Linear model

For the stable grinding process, $(x_g(\tau), x_p(\tau), y_p(\tau))$ should be stabilized at (x_{g0}, x_{p0}, y_{p0}). To discuss the stability of the steady grinding, the system is linearised at (x_{g0}, x_{p0}, y_{p0}) by introducing

$$\mathbf{X}(\tau) = \epsilon \begin{pmatrix} x_1(\tau) \\ x_2(\tau) \\ x_3(\tau) \end{pmatrix} = \begin{pmatrix} x_g(\tau) \\ x_p(\tau) \\ y_p(\tau) \end{pmatrix} - \begin{pmatrix} x_{g0} \\ x_{p0} \\ y_{p0} \end{pmatrix}, \tag{18}$$

where ϵ is a small dimensionless parameter, which means that the fluctuations of $\mathbf{X}(\tau)$ are relatively small. Moreover, from Eqs. 9 and 14, it is known that the contact angle γ, the grinding depth d_g, and the delays τ_w and τ_g are nonlinear functions of $(x_1(\tau), x_2(\tau), x_3(\tau))^{\mathrm{T}}$, and they should be linearised first.

To begin with, the contact angle γ is linearised by substituting (18) into Eq. 14 yielding

$$\gamma = \tan^{-1}\left(\frac{y_{p0} + \epsilon x_3(\tau)}{1 - \nu - x_{p0} - \epsilon x_2(\tau) + x_{g0} + \epsilon x_1(\tau)}\right). \tag{19}$$

Then, γ is expanded in a Taylor's series as:

$$\gamma \approx \gamma_0 + \epsilon \gamma_1, \tag{20}$$

where

$$\gamma_1 = \frac{y_{p0}(x_2(\tau) - x_1(\tau)) + (1 - \nu + x_{g0} - x_{p0}) x_3(\tau)}{(1 - \nu + x_{g0} - x_{p0})^2 + y_{p0}^2} \tag{21}$$

is the linear part of γ.

Next, Eqs. 18 and 21 are substituted into Eq. 9 to linearise the time delays, τ_w and τ_g, which yields

$$\begin{aligned}
2\pi &= -\epsilon\gamma_1(\tau) + \epsilon\gamma_1(\tau - \tau_w) + \tau_w \omega_w, \\
2\pi &= \epsilon\gamma_1(\tau) - \epsilon\gamma_1(\tau - \tau_g) + \tau_g \omega_g.
\end{aligned} \tag{22}$$

Clearly, Eq. 22 is a transcendental equation with respect to τ_w and τ_g. Thus, the perturbation method is used for the linear approximation [28]. Expanding τ_w and τ_g into

$$\begin{aligned}
\tau_w &= \tau_{w0} + \epsilon\tau_{w1} + o(\epsilon), \\
\tau_g &= \tau_{g0} + \epsilon\tau_{g1} + o(\epsilon),
\end{aligned} \tag{23}$$

substituting (23) into Eq. 22, expanding the equation in a Taylor's series, and collecting coefficients of ϵ^0 and ϵ^1 leads to

$$\begin{aligned}
2\pi &= \omega_w \tau_{w0}, \\
2\pi &= \omega_g \tau_{g0},
\end{aligned} \tag{24}$$

and

$$\begin{aligned}
0 &= -\gamma_1(\tau) + \gamma_1(\tau - \tau_{w0}) + \omega_w \tau_{w1}, \\
0 &= \gamma_1(\tau) - \gamma_1(\tau - \tau_{g0}) + \omega_g \tau_{g1}.
\end{aligned} \tag{25}$$

Solving the above equations results in

$$\begin{aligned}\tau_{w0} &= \frac{2\pi}{\omega_w},\\ \tau_{g0} &= \frac{2\pi}{\omega_g},\\ \tau_{w1} &= \frac{1}{\omega_w}\left(\gamma_1(\tau)-\gamma_1(\tau-\tau_{w0})\right),\\ \tau_{g1} &= \frac{1}{\omega_g}\left(-\gamma_1(\tau)+\gamma_1(\tau-\tau_{g0})\right).\end{aligned} \tag{26}$$

Here, τ_{w0} and τ_{g0} are constant time delays with respect to the grinding without considering the vertical workpiece motion [19, 24, 46, 48].

To find the linear grinding depth, Eqs. 18, 21 and 26 are substituted into Eq. 14, before the Taylor's series expansion is applied to obtain

$$d_g \approx d_{g0} + \epsilon d_{g1}, \tag{27}$$

where the linear part of the regenerative grinding depth is given by

$$\begin{aligned}d_{g1} = {} & \frac{(1-\nu+x_{g0}-x_{p0})^3+(x_{g0}-x_{p0})y_{p0}^2}{\left((1-\nu+x_{g0}-x_{p0})^2+y_{p0}^2\right)^{\frac{3}{2}}}\times\\ & \left(x_p(\tau)-x_p(\tau-\tau_{w0})-x_g(\tau)+x_g(\tau-\tau_{w0})\right)\\ & -\frac{(1-\nu+x_{g0}-x_{p0})(2-2\nu+x_{g0}-x_{p0})y_{p0}+y_{p0}^3}{\left((1-\nu+x_{g0}-x_{p0})^2+y_{p0}^2\right)^{\frac{3}{2}}}\times\\ & \left(y_p(\tau)-y_p(\tau-\tau_{w0})\right)\\ & +\frac{\nu y_{p0}^2}{\left((1-\nu+x_{g0}-x_{p0})^2+y_{p0}^2\right)^{\frac{3}{2}}}\left(x_g(\tau)-x_p(\tau)\right)\\ & -\frac{\nu(1-\nu+x_{g0}+x_{p0})y_{p0}}{\left((1-\nu+x_{g0}-x_{p0})^2+y_{p0}^2\right)^{\frac{3}{2}}}y_p(\tau).\end{aligned} \tag{28}$$

Finally, by substituting (20), (21), (23), (26), (27) and (28), into Eq. 15, one obtains the linear model of the grinding

$$\mathbf{M}\frac{\mathrm{d}^2\mathbf{X}(\tau)}{\mathrm{d}\tau^2}+\mathbf{C}\frac{\mathrm{d}\mathbf{X}(\tau)}{\mathrm{d}\tau}+\mathbf{K}\mathbf{X}(\tau)=\mathbf{A}\mathbf{V}(\tau), \tag{29}$$

where

$$\mathbf{V}(\tau)=\begin{pmatrix}\gamma_1\\ d_{g1}\\ \frac{\mathrm{d}\gamma_1}{\mathrm{d}\tau}\end{pmatrix}=\mathbf{D}\mathbf{X}(\tau)+\mathbf{D}_w\mathbf{X}(\tau-\tau_{w0})+\mathbf{D}_g\mathbf{X}(\tau-\tau_{g0})+\mathbf{D}_v\frac{\mathrm{d}\mathbf{X}(\tau)}{\mathrm{d}\tau}. \tag{30}$$

The elements of the coefficient matrices, **M**, **C**, **K**, **A**, **D**, $\mathbf{D}_w$, $\mathbf{D}_g$ and $\mathbf{D}_v$, are given in Appendix. B.

3.3 Stability boundaries

The linear stability of the grinding is determined by the eigenvalues of Eq. 29 which can be obtained by solving the following eigenvalue equation

$$\left|\lambda^2\mathbf{M}+\lambda(\mathbf{C}-\mathbf{A}\mathbf{D}_v)+(\mathbf{K}-\mathbf{A}\mathbf{D})-\mathbf{A}\mathbf{D}_w e^{-\lambda\tau_{w0}}-\mathbf{A}\mathbf{D}_g e^{-\lambda\tau_{g0}}\right|=0, \tag{31}$$

where λ represents the eigenvalue and $|\bullet|$ the determinant of the matrix $\bullet$. If all the solutions of Eq. 31 have negative real parts, the grinding is stable. In case of any λ has a positive real part, a chatter occurs. Thus, to locate the stability boundary and divide the chatter-free and the chatter regions, $\lambda = \pm i\omega$ is substituted into Eq. 31 and its real and imaginary parts are separated [47]:

$$\begin{aligned}\Re\left(\left|-\omega^2\mathbf{M}+i\omega(\mathbf{C}-\mathbf{A}\mathbf{D}_v)+(\mathbf{K}-\mathbf{A}\mathbf{D})-\mathbf{A}\mathbf{D}_w e^{-i\omega\tau_{w0}}-\mathbf{A}\mathbf{D}_g e^{-i\omega\tau_{g0}}\right|\right)=0,\\ \Im\left(\left|-\omega^2\mathbf{M}+i\omega(\mathbf{C}-\mathbf{A}\mathbf{D}_v)+(\mathbf{K}-\mathbf{A}\mathbf{D})-\mathbf{A}\mathbf{D}_w e^{-i\omega\tau_{w0}}-\mathbf{A}\mathbf{D}_g e^{-i\omega\tau_{g0}}\right|\right)=0,\end{aligned} \tag{32}$$

where $\Re(\bullet)$ and $\Im(\bullet)$ indicate real and imaginary parts of $\bullet$, respectively. It is worth reiterating here that Eq. 32 is transcendental and does not have readily available analytical solutions. Thus, a numerical continuation algorithm is employed to determine the stability boundary [29]. Details of the algorithm are presented in Appendix C.

As an example, parameter values used in the following analyses are listed in Table 2.

By using the eigenvalue calculation and the continuation algorithm, the stability *lobes*, i.e. the stability boundaries, are obtained [1, 4, 24, 25]. As illustrated in Fig. 9, the boundaries divide the $\tau_{w0} - w$ plane into two parts. Specifically, the up-left part is white, indicating the chatter region for small τ_{w0} and large w. By contrast, the grey region is the bottom-right part, corresponding to chatter-free grinding process with respect to large τ_{w0} and small w.

4 Grinding stability analysis of the full model

When the workpiece mass is uniformly distributed and its imbalance is ignorable ($\delta = 0$), Eq. 15 is similar to the system analysed in our previous work [46, 47]. In that case, there is no forced vibration in the grinding process and only the self-induced chatter can be found. If the imbalance is involved ($\delta > 0$), by contrast, the chatter is interrupted and various grinding dynamics can occur. To illustrate this point, the system parameters corresponding to arrows I, II,

Table 2 Parameter values selected for further linear and nonlinear analyses

Parameters	Symbols	Values
Mass density [kg m^{-3}]	ρ	7850
Wheel mass [kg]	m_g	30
Young's modulus [Pa]	E	2.06×10^{11}
Wheel stiffness [N m^{-1}]	k_g	7×10^6
Workpiece length [m]	L	1
Workpiece radius [m]	R_w	0.01
Wheel radius [m]	R_g	0.15
Disc radius [m]	R_d	0.1
Wheel position [m]	P	0.5
Workpiece damping [N s m^{-1}]	c_w	1.2×10^3
Wheel damping [N s m^{-1}]	c_g	1.0×10^4
Feed [m rev^{-1}]	f	0.001
Wheel period [s]	T_g	0.027
Dimensionless ratio [-]	ψ	1.786
Dimensionless ratio [-]	g	0.02
Friction coefficient [-]	μ_d	1

III and IV are selected (see Fig. 9), and their dynamics is investigated next.

4.1 Forced vibration in the grinding

To begin with, an extensive numerical simulation of the grinding process along arrow I is performed for the maximum grinding depth max(d_g), see example result shown in Fig. 10a. As arrow I is located in the chatter-free region, there is no chatter vibration and max(d_g) confirms the stable grinding. This is seen in Fig. 10b ($\tau_{w0} = 10$), where the initial fluctuation of d_g is quickly damped down.

No self-excited chatter is found on arrow I, since it is located in the chatter-free region. Without other source of vibration, one can anticipate a stable grinding process. If the mass eccentricity of the workpiece is involved, the forced vibration would arise according to Eq. 15. To illustrate, both small ($\delta = 0.1$) and large ($\delta = 1.0$) imbalances are introduced, and corresponding results are plotted in Fig. 11. As can be seen, a larger eccentricity (Fig. 11b) generally yields a larger vibration amplitude (Fig. 11a). Moreover, with respect to the increase of τ_{w0}, it shows a descent of the vibration amplitude. This is attributed to the excitations in Eq. 15, $\frac{\delta}{\tau_{w0}^2}\sin\left(\frac{2\pi}{\tau_{w0}}\tau\right)$ and $\frac{\delta}{\tau_{w0}^2}\cos\left(\frac{2\pi}{\tau_{w0}}\tau\right)$, which are in an inverse square relationship with τ_{w0}.

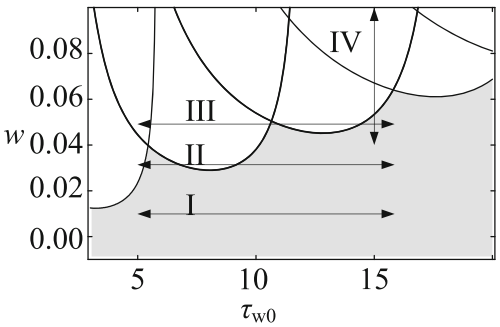

Fig. 9 Stability boundaries for the grinding process without the workpiece imbalance effect plotted in $\tau_{w0} - w$ plane. The boundaries divide the region into *white and grey* regions, which correspond to the chatter and chatter-free regions, respectively. The *lines with double arrows* marked by I ($w = 0.01$, $\tau_{w0} \in [5, 16]$), II ($w = 0.033$, $\tau_{w0} \in [5, 16]$), II ($w = 0.048$, $\tau_{w0} \in [5, 16]$) and IV ($\tau_{w0} = 15$, $\tau_{w0} \in [0.04, 0.1]$) will be used for further analysis presented in the next section

4.2 Grinding dynamics without imbalance

Next investigation of the grinding dynamics is along arrow II region shown in Fig. 12. Unlike for the system parameters corresponding to arrow I, it crosses the stability boundaries

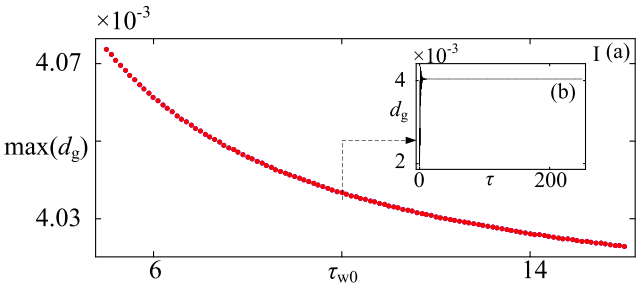

Fig. 10 Dependence of the grinding depth on τ_{w0}. The system parameters correspond to arrow I marked in Fig. 9 ($w = 0.1$, $\tau_{w0} \in [5, 16]$). **b** The stable grinding process for $\tau_{w0} = 10$ is displayed in an extra window

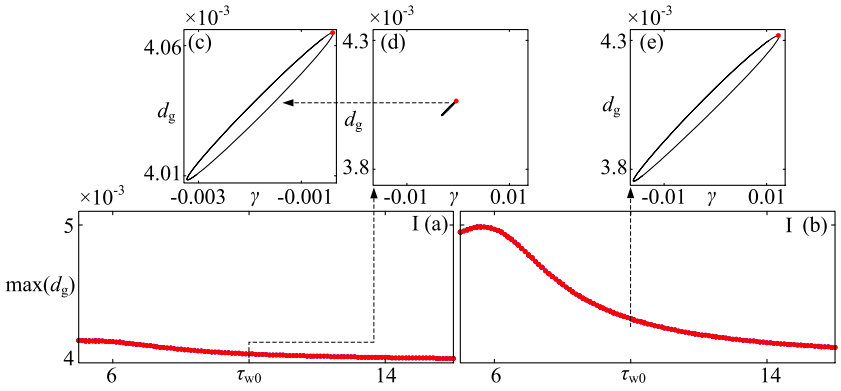

Fig. 11 Dependence of the grinding depth on τ_{w0} when the workpiece imbalance is considered. The system parameters vary along arrow I marked in Fig. 9 ($w = 0.1$, $\tau_{w0} \in [5, 16]$). Panels (**a**) and (**b**) show the system responses for small ($\delta = 0.1$) and large ($\delta = 1.0$) workpiece imbalances, respectively

for three times, and thus both the stable grinding and the chatter are anticipated to be observed. More specifically, arrow II region has its left end in the chatter region and its right end in the chatter-free one. In addition, it crosses another *lobe* near it left end ($w = 0.033$ and $\tau_{w0} \in [6.4, 9.5]$). A corresponding bifurcation diagram is depicted in Fig. 12a, where blue dots indicate $\max(d_g)$ obtained from a brute force forward numerical simulation (τ_{w0} increases from 5 to 16), and red dots are from a backward simulation (τ_{w0} decreases from 16 to 5). Similarly to the investigations carried out in [46], we also observe a co-existence of a stable grinding and a large-amplitude chatter. That is to say, the chatter is induced by a sub-critical Hopf bifurcation [45, 46]. More information of the co-existence are given in Fig. 12b–f. Two chatter motions predicted for $\tau_{w0} = 5.5$ are depicted in Fig. 12b, d, while the chatter and chatter-free grinding cases predicted for $\tau_{w0} = 10$ are shown in Fig. 12c and f.

In the bifurcation analysis, both forward and backward simulations are employed to reveal the bi-stability in the grinding process. As known, nonlinearity can introduce coexisting dynamics, and long-term motion of a system

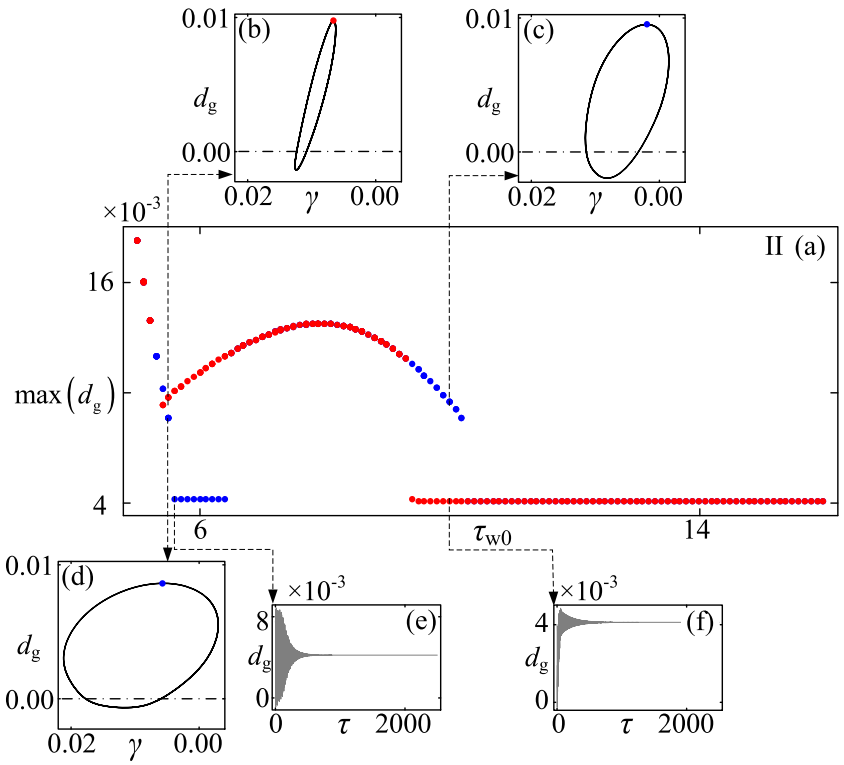

Fig. 12 Dependence of the grinding depth on τ_{w0}. The system parameters vary along arrow II marked in Fig. 9 ($w = 0.033$, $\tau_{w0} \in [5, 16]$). *Blue and red dots* indicate the results from forward and backward simulations, respectively

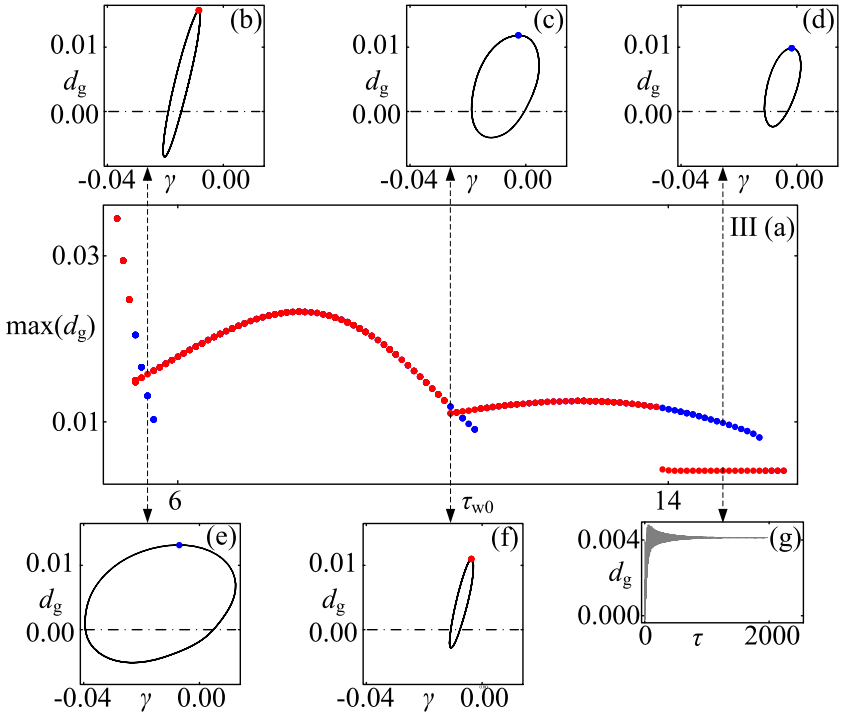

Fig. 13 Dependence of the grinding depth on τ_{w0}. The system parameters vary along arrow III marked in Fig. 9 ($w = 0.048$, $\tau_{w0} \in [5, 16]$). *Blue and red dots* indicate the results from forward and backward simulations, respectively

is determined by its initial condition. In metal cutting processes, the bi-stability exists extensively. For example, Molnár et al. recently carried out an investigation of bi-stability in a turning process, where all the bi-stable zones for both stable and unstable processes were theoretically predicted [27]. In our bifurcation analysis with numerical simulations, the forward and backward simulations are techniques to generate different initial conditions for different attractors. To illustrate, Fig. 12b, d show two different chatter motions for $\tau_{w0} = 5.5$. To obtain the two motions in the simulation, the initial condition for Fig. 12b is from the red dot on its right side (backward), while the motion in Fig. 12d is started from the blue dot on its left side (forward).

For the bifurcation analysis along arrow III, the width is increased from $w = 0.033$ to 0.048, and the bifurcation diagram is depicted in Fig. 13a. Except the co-existence of the stable and unstable grinding (see Fig. 13d, g computed for $\tau_{w0} = 15$), we also observe the co-existence of different grinding chatter vibrations, which are shown in Fig. 13b, e computed for $\tau_{w0} = 5.5$, and Fig. 13c, f computed for $\tau_{w0} = 10.5$. Moreover, another general trend shown in Fig. 13 is a decrease of max(d_g) with respect to τ_{w0}. Following the forward simulation, the chatter amplitudes in Fig. 13e, c d decreases with respect to the increase of τ_{w0}.

The influence of the contact width w on the grinding dynamics is analysed by numerical simulations along arrow IV. As can be seen in Fig. 14, a simple sub-critical Hopf bifurcation features here. The grinding process keeps its linear stability for a small grinding width ($w < 0.54$), and a large-amplitude chatter arises suddenly when w exceeds a critical value. In the backward sweep (w decreases from 0.1 to 0.01), the grinding chatter in the chatter-free region is observed as well, yielding a co-existence of the stable and unstable grinding. This phenomenon is depicted in Fig. 14b and c, corresponding to the chatter and chatter-free grinding, respectively.

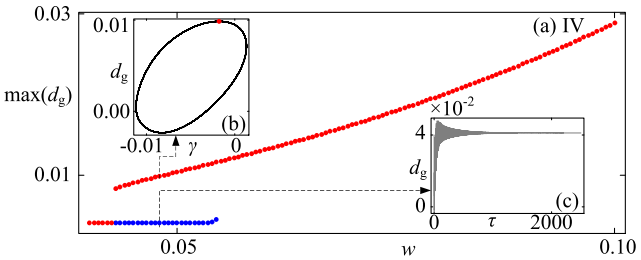

Fig. 14 Dependence of the grinding depth on w. The system parameters vary along arrow IV marked in Fig. 9 ($\tau_{w0} = 3$, $w \in [0.01, 0.1]$). *Blue and red dots* indicate the results from forward and backward simulations, respectively

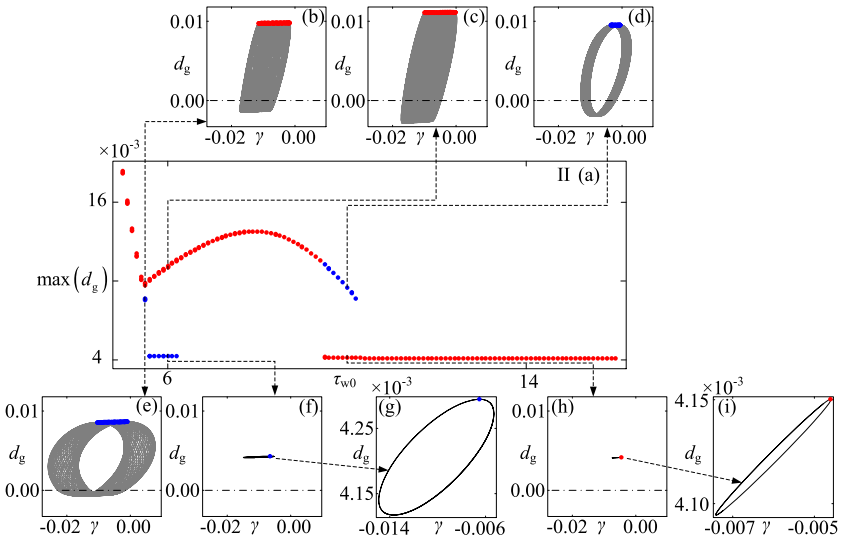

Fig. 15 Dependence of the grinding depth on τ_{w0} when small workpiece imbalance ($\delta = 0.1$) is considered. The system parameters vary along arrow II marked in Fig. 9 ($w = 0.033$, $\tau_{w0} \in [5, 16]$). *Blue and red dots* indicate the results from forward and backward simulations, respectively

4.3 Grinding dynamics with workpiece imbalance

Here, both effects of the workpiece imbalance and the regeneration are considered, so that the dynamic interactions between the forced and the self-excited vibrations can be investigated. Firstly, a small workpiece imbalance ($\delta = 0.1$) is introduced for the system parameters along arrow II. The corresponding bifurcation diagram is shown in Fig. 15, where the system response varies with respect to τ_{w0} as shown in Fig. 15a and it is very similar to that in Fig. 12a with one difference as the periodic chatter is transformed into quasi-periodic one and the stable grinding becomes oscillatory. These phenomena can be better understood by comparing Fig. 12b, f with Fig. 15b, h. In addition, the amplitude decrease of the forced vibration with respect to an increase of τ_{w0}, as depicted in Fig. 15f, h, demonstrates the same trend as that in Fig. 11.

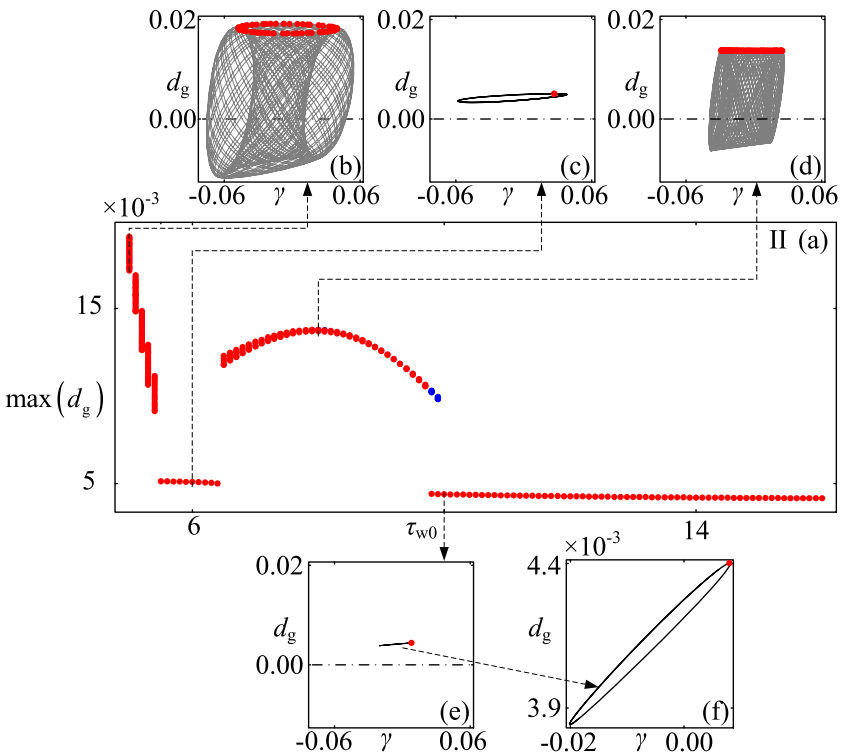

Fig. 16 Dependence of the grinding depth on τ_{w0} when large workpiece imbalance ($\delta = 1.0$) is considered. The system parameters vary along arrow II marked in Fig. 9 ($w = 0.033$, $\tau_{w0} \in [5, 16]$). *Blue and red dots* indicate the results from forward and backward simulations, respectively

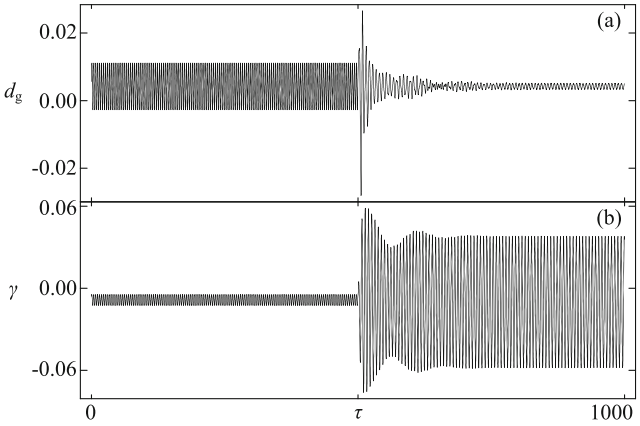

Fig. 17 Time histories of the grinding chatter, which is quench by the large workpiece imbalance for $w = 0.033$ and $\tau_{w0} = 6$. No imbalance is considered before $\tau = 500$, and $\delta = 1.0$ is introduced thereafter

Next, a large workpiece imbalance ($\delta = 1.0$) is considered and the corresponding bifurcation pattern is depicted in Fig. 16. Here, one can see a shrink of the regions for the co-existing attractors. More specifically, the co-existence between the quasi-periodic chatter and the forced vibration is observed only for $\tau_{w0} \in [9.8, 9.9]$. Moreover, it is seen that the large-amplitude chatter for $\tau_{w0} \in [5.5, 6.4]$ is quenched by the large workpiece imbalance. Comparing Fig. 16c with Fig. 15c, one can deduct that the fluctuation of the grinding depth d_g is dramatically decreased, so that no losing contact between the wheel and the workpiece is seen (d_g is positive). Meanwhile, the vibration amplitude of the contact angle γ grows sharply. This transformation is clearly displayed in Fig. 17, where there is no imbalance for $\tau \in [0, 500]$ but $\delta = 1.0$ for $\tau \in (500, 1000]$. By reviewing our previous works [44, 47], one can see that the grinding chatter can be quenched by various harmonic perturbations including spindle speed variation (SSV) and the workpiece imbalance.

For the large imbalance unchanged at $\delta = 1.0$, the grinding dynamics along arrow III is discussed next. The bifurcation diagram and its corresponding phase portraits are plotted in Fig. 18. This bifurcation pattern can be regarded as a perturbation of that depicted in Fig. 13. However, unlike the grinding chatter in Fig. 16, $\delta = 1.0$ is not large enough to quench the grinding chatter with a large contact width ($w = 0.048$), so only quasi-periodic chatter and a periodic forced vibration are seen.

Finally, we consider the grinding dynamics along arrow IV. Unlike those along arrows I, II and III, arrow IV is for a fixed value of τ_{w0}, so that the frequency of the excitations due to the imbalance, $\frac{\delta}{\tau_{w0}^2}\sin\left(\frac{2\pi}{\tau_{w0}}\tau\right)$ and $\frac{\delta}{\tau_{w0}^2}\cos\left(\frac{2\pi}{\tau_{w0}}\tau\right)$, are constant. However, the variation of w results in change of the chatter frequency. One may find a specific value of w for a rational frequency ratio, and thus a periodic chatter, instead of the quasi-periodic one, can be observed. And a such response is shown Fig. 19, where the bifurcation diagram of $\max(\gamma)$ is added for a clearer illustration. As seen in Fig. 19b, most cases of the grinding chatter along arrow IV are quasi-periodic. On both sides of $\tau_{w0} = 0.087$, as shown in Fig. 19c, d, the quasi-periodic chatter is obtained. However, as seen in Fig. 19b, a periodic window shows up in the vicinity of $\tau_{w0} = 0.087$, and thus a periodic phase portrait is observed in Fig. 19g.

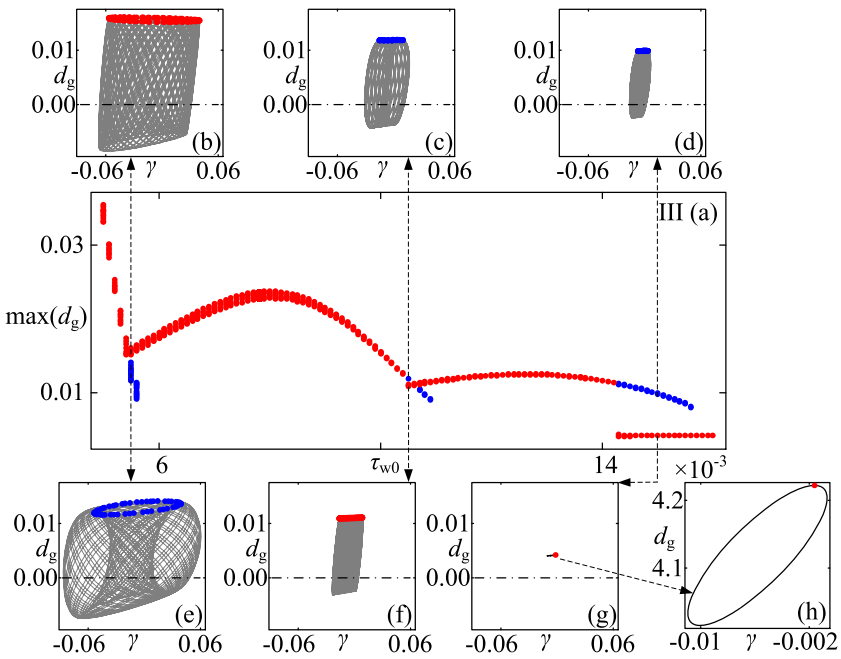

Fig. 18 Dependence of the grinding depth on τ_{w0} when large workpiece imbalance ($\delta = 1.0$) is considered. The system parameters vary along arrow III marked in Fig. 9 ($w = 0.048$, $\tau_{w0} \in [5, 16]$). *Blue and red dots* indicate the results from forward and backward simulations, respectively

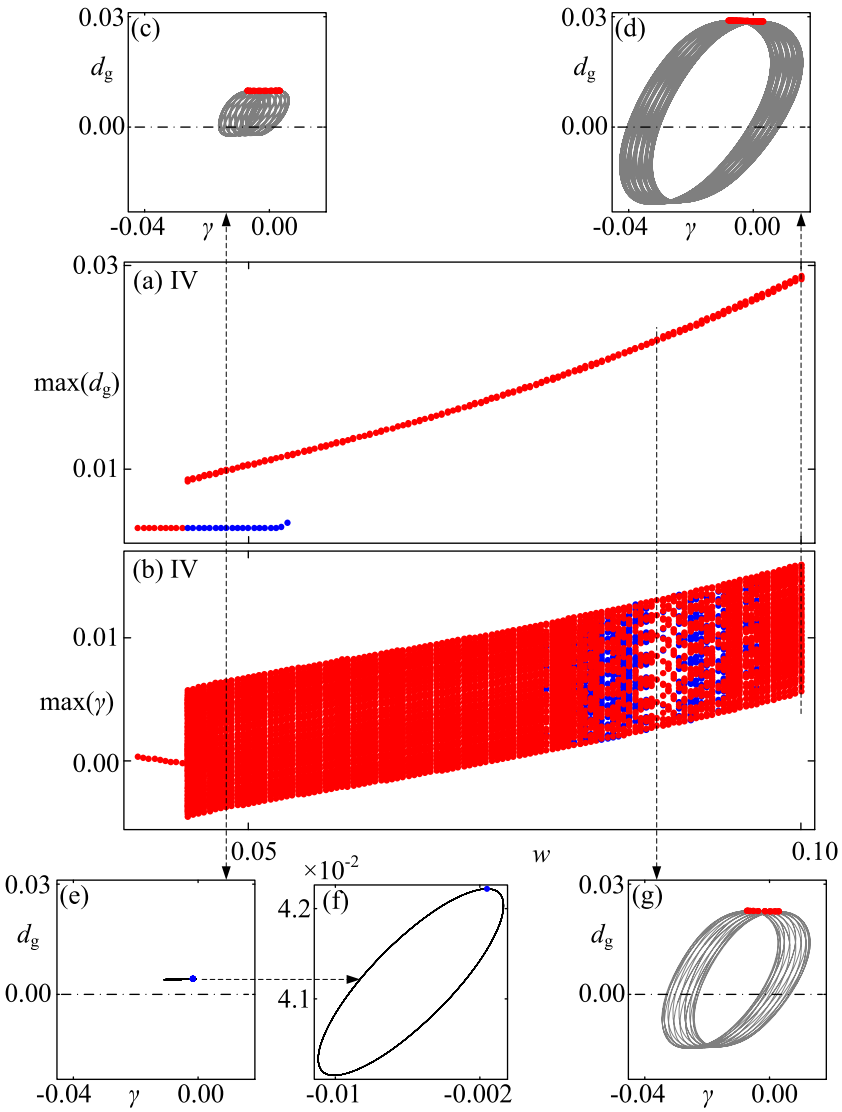

Fig. 19 Dependence of the grinding depth on w when large workpiece imbalance ($\delta = 1.0$) is considered. The system parameters vary along arrow IV marked in Fig. 9 ($\tau_{w0} = 3$, $w \in [0.01, 0.1]$). *Blue and red dots* indicate the results from forward and backward simulations, respectively

5 Conclusions

In this paper, we aimed to obtain a further insight into the stability of the grinding dynamics, a model involving the wheel-workpiece regeneration and the workpiece imbalance was proposed. More specifically, time delays were employed to represent the regenerative effect, and the rotor dynamics of the workpiece imbalance was included as well. Such a model involving the planar motion of the workpiece and the horizontal wheel movement. The resulting normal cutting and the tangential frictional forces were modelled, and the state-dependent time delays were used to analyse regenerative effect. Based on this model, the grinding stability for the cases with and without workpiece imbalance were studied.

The stability was numerically evaluated by eigenvalue and continuation calculations gradually increasing the complexity of the model being analysed. Firstly, the external exciting was neglected to undertake linear stability analysis which proved stability boundaries in the form of stability lobes dividing the parameter plane for chatter-free and chatter regions. It was shown that the grinding stability can be undermined by the increase of the grinding width W or the rotary speed of the workpiece Ω_w.

Next, the self-induced and the external-excited grinding vibrations were investigated through a numerical simulation. In case of a small grinding width ($w = 0.01$), we have a chatter-free behaviour, which can be accredited to the workpiece imbalance. For large grinding width, the vibration is attributed to regenerative chatter. Moreover, it was observed that the chatter strength is enhanced by the increase of the grinding width or the workpiece speed.

Lastly, the combination of the regenerative grinding chatter and the rotor dynamics was considered. With a small imbalance, the bifurcation patterns of the chatter were almost unchanged, but the original period chatter was

transformed into quasi-periodic one, and the chatter-free grinding becomes forced vibration with a small amplitude. When the large imbalance ($\delta = 1.0$) was involved, the fluctuation amplitude of the contact angle was increased. Specially, the large-amplitude chatter in the linearly chatter-free region can be quenched by the rotor dynamics, leaving a forced vibration with small amplitude in the grinding depth but large amplitude in the contact angle. With a fixed τ_{w0}, the frequency of the external exciting is constant, and in this case, one can choose a a specific value of w to find a periodic, instead of other quasi-periodic chatter with a workpiece imbalance.

Acknowledgments This research is supported by the National Natural Science Foundation of China under Grant No. 11572224 and 11502048, and Fundamental Research Funds for the Central Universities under Grant No.ZYGX2015KYQD033.

Appendix A Coefficients of the discrete model

Considering bending motions of the workpiece, the wheel and the disc, the kinetic energy can be described as

$$\begin{aligned} T = {} & \int_0^L \tfrac{1}{2}\rho\pi r_w^2 \left(\left(\frac{dX_w(t,S)}{dt} \right)^2 + \left(\frac{dY_w(t,S)}{dt} \right)^2 \right) dS \\ & + \tfrac{1}{2} m_d \left(\frac{d(X_w(t,P) + e\cos(\Omega_w t))}{dt} \right)^2 \\ & + \tfrac{1}{2} m_d \left(\frac{d(Y_w(t,P) + e\sin(\Omega_w t))}{dt} \right)^2 + \tfrac{1}{2} m_g \left(\frac{dX_g(t)}{dt} \right)^2. \end{aligned} \tag{33}$$

Assuming the linear elasticity theory to describe the potential energy of the workpiece and the wheel holder, one can obtain

$$\begin{aligned} V = {} & \tfrac{1}{2}\int_0^L \left(EI \left(\frac{d^2X_w(t,S)}{dS^2} \right)^2 + EI \left(\frac{d^2Y_w(t,S)}{dS^2} \right)^2 \right) dS \\ & + \tfrac{1}{2} k_g \left(\frac{dX_g(t)}{dt} \right)^2, \end{aligned} \tag{34}$$

where $I = \pi r_w^4/4$ is the area moment of inertia of cross-section of the workpiece. In addition, inherent material damping and inter-facial damping of the grinding are considered and represented by a equivalent dissipation function described by [23]

$$D = \frac{1}{2} \left(c_w \left(\frac{dX_p}{dt} \right)^2 + c_w \left(\frac{dY_p}{dt} \right)^2 + c_g \left(\frac{dX_g}{dt} \right)^2 \right), \tag{35}$$

where c_w is the equivalent viscous damping coefficient with respect to workpiece bending, and c_g is that of the wheel.

For simplicity, the bending displacement of the workpiece in the x direction is assumed as

$$X_w(t,S) = \begin{cases} a_{x0}(t) + a_{x1}(t)S + a_{x2}(t)S^2 + a_{x3}(t)S^3 & \text{, if } 0 \le S \le P, \\ b_{x0}(t) + b_{x1}(t)S + b_{x2}(t)S^2 + b_{x3}(t)S^3 & \text{, if } P \le S \le L, \end{cases} \tag{36}$$

where a_{xi} and b_{xi} $(i = 0, 1, 2, 3)$ vary with respect to time. Furthermore, boundary conditions with respect to $X_w(t, S)$ are

$$\begin{cases} X_w(t,0) = 0, \\ \frac{dX_w(t,0)}{dS} = 0, \\ X_w(t,S)\,|_{S\to P^-} = X_p(t), \\ X_w(t,S)\,|_{S\to P^+} = X_p(t), \\ \frac{dX_w(t,S)}{dS}\,|_{S\to P^-} = \frac{dX_w(t,S)}{dS}\,|_{S\to P^+}, \\ \frac{d^2X_w(t,S)}{dS^2}\,|_{S\to P^-} = \frac{d^2X_w(t,S)}{dS^2}\,|_{S\to P^+}, \\ X_w(t,L) = 0, \\ \frac{d^2X_w(t,0)}{dS^2} = 0, \end{cases} \tag{37}$$

where $X_p(t) = X_w(t, P)$ is the horizontal displacement of the disc. Substituting (36) into Eq. 37, and solving for a_{xi} and b_{xi} $(i = 0, 1, 2, 3)$ yield

$$X_w(t,S) = \begin{cases} \frac{3L(2L-P)PS^2 + (P^2-2LP-2L^2)S^3}{P^3(4L-P)(L-P)} X_p(t), & \text{if } 0 \le S \le P, \\ \frac{-2L^3P + 6L^3S + 3L(P-3L)S^2 + (3L-P)S^3}{(L-P)^2P(4L-P)} X_p(t), & \text{if } P \le S \le L. \end{cases} \tag{38}$$

Similarly, $Y_w(t, S)$ is represented by

$$Y_w(t,S) = \begin{cases} \frac{3L(2L-P)PS^2 + (P^2-2LP-2L^2)S^3}{P^3(4L-P)(L-P)} Y_p(t), & \text{if } 0 \le S \le P, \\ \frac{-2L^3P + 6L^3S + 3L(P-3L)S^2 + (3L-P)S^3}{(L-P)^2P(4L-P)} Y_p(t), & \text{if } P \le S \le L, \end{cases} \tag{39}$$

where $Y_p(t) = Y_w(t, P)$ is the vertical displacement of the disc.

Next, the governing equation of the grinding is obtained by Lagrange's equations

$$\frac{d}{dt}\frac{\partial L}{\partial (dq_i/dt)} - \frac{\partial L}{\partial q_i} + \frac{\partial D}{\partial (dq_i/dt)} = Q_{q_i}, \tag{40}$$

where the Largrange L is $L = T - V$, q_i represents generalized coordinates, $X_g(t)$, $X_p(t)$ and $Y_p(t)$, and Q_{q_i} indicates corresponding generalized forces. Substituting (33), (34), (35), (38) and (39) into Eq. 40 yields (2), where the equivalent stiffness and mass for the workpiece are:

$$\begin{aligned} k_w = {} & \frac{12EIL^3}{(L-P)^2(4L-P)P^3}, \\ m_w = {} & \frac{70m_dP^2(4L^2-5LP+P^2)^2}{35(L-P)^2P^2(4L-P)^2} \\ & + \frac{\pi\rho L^3R_w^2(24L^4-24L^3P-4L^2P^2+8LP^3-P^4)}{35(L-P)^2P^2(4L-P)^2}, \end{aligned} \tag{41}$$

Appendix B Coefficient matrices

The linear part of the dimensionless governing equation of the grinding, Eq. 29, has the coefficient matrices **M**, **C**, **K** and **A** given by

$$\mathbf{M}=\begin{pmatrix}1&0&0\\0&1&0\\0&0&1\end{pmatrix},\quad \mathbf{C}=\begin{pmatrix}\xi_{\mathrm{g}}&0&0\\0&\xi_{\mathrm{w}}&0\\0&0&\xi_{\mathrm{w}}\end{pmatrix},\quad \mathbf{K}=\begin{pmatrix}\kappa_{\mathrm{g}}&0&0\\0&1&0\\0&0&1\end{pmatrix},\quad \mathbf{A}=\left(a_{ij}\right)_{3\times 3}, \tag{42}$$

where

$$\begin{aligned}
a_{11} &= w\kappa_{\mathrm{f}}\tfrac{\tau_{\mathrm{g}0}}{\tau_{\mathrm{w}0}}\sqrt{d_{\mathrm{g}0}}\left(\mu\cos(\gamma_0)-\sin(\gamma_0)\right)+w\kappa_{\mathrm{c}}\tfrac{\tau_{\mathrm{g}0}}{\tau_{\mathrm{w}0}}d_{\mathrm{g}0}\left(\psi\cos(\gamma_0)-\sin(\gamma_0)\right),\\
a_{12} &= w\kappa_{\mathrm{f}}\tfrac{\tau_{\mathrm{g}0}}{\tau_{\mathrm{w}0}}\tfrac{1}{2\sqrt{d_{\mathrm{g}0}}}\left(\cos(\gamma_0)+\mu\sin(\gamma_0)\right)+w\kappa_{\mathrm{c}}\tfrac{\tau_{\mathrm{g}0}}{\tau_{\mathrm{w}0}}\left(\cos(\gamma_0)+\psi\sin(\gamma_0)\right),\\
a_{13} &= -w\kappa_{\mathrm{f}}\tfrac{\tau_{\mathrm{g}0}(\tau_{\mathrm{g}0}+\tau_{\mathrm{w}0})}{2\pi\tau_{\mathrm{w}0}}\sqrt{d_{\mathrm{g}0}}\left(\cos(\gamma_0)+\mu\sin(\gamma_0)\right)\\
&\quad -w\kappa_{\mathrm{c}}\tfrac{\tau_{\mathrm{g}0}(\tau_{\mathrm{g}0}+\tau_{\mathrm{w}0})}{2\pi\tau_{\mathrm{w}0}}d_{\mathrm{g}0}\left(\cos(\gamma_0)+\psi\sin(\gamma_0)\right),\\
a_{21} &= -\tfrac{a_{11}}{\gamma_{\mathrm{w}}},\quad a_{22}=-\tfrac{a_{12}}{\gamma_{\mathrm{w}}},\quad a_{23}=-\tfrac{a_{13}}{\gamma_{\mathrm{w}}},\\
a_{31} &= \tfrac{w\kappa_{\mathrm{f}}}{\gamma_{\mathrm{w}}}\tfrac{\tau_{\mathrm{g}0}}{\tau_{\mathrm{w}0}}\sqrt{d_{\mathrm{g}0}}\left(\cos(\gamma_0)+\mu\sin(\gamma_0)\right)+\tfrac{w\kappa_{\mathrm{c}}}{\gamma_{\mathrm{w}}}\tfrac{\tau_{\mathrm{g}0}}{\tau_{\mathrm{w}0}}d_{\mathrm{g}0}\left(\cos(\gamma_0)+\psi\sin(\gamma_0)\right),\\
a_{32} &= \tfrac{w\kappa_{\mathrm{f}}}{\gamma_{\mathrm{w}}}\tfrac{\tau_{\mathrm{g}0}}{\tau_{\mathrm{w}0}}\tfrac{1}{2\sqrt{d_{\mathrm{g}0}}}\left(\sin(\gamma_0)-\mu\cos(\gamma_0)\right)+\tfrac{w\kappa_{\mathrm{c}}}{\gamma_{\mathrm{w}}}\tfrac{\tau_{\mathrm{g}0}}{\tau_{\mathrm{w}0}}\left(\sin(\gamma_0)-\psi\cos(\gamma_0)\right),\\
a_{33} &= \tfrac{w\kappa_{\mathrm{f}}}{\gamma_{\mathrm{w}}}\tfrac{\tau_{\mathrm{g}0}(\tau_{\mathrm{g}0}+\tau_{\mathrm{w}0})}{2\pi\tau_{\mathrm{w}0}}\sqrt{d_{\mathrm{g}0}}\left(\mu\cos(\gamma_0)-\sin(\gamma_0)\right)\\
&\quad +\tfrac{w\kappa_{\mathrm{c}}}{\gamma_{\mathrm{w}}}\tfrac{\tau_{\mathrm{g}0}(\tau_{\mathrm{g}0}+\tau_{\mathrm{w}0})}{2\pi\tau_{\mathrm{w}0}}d_{\mathrm{g}0}\left(\psi\cos(\gamma_0)-\sin(\gamma_0)\right).
\end{aligned} \tag{43}$$

The matrix, **D**, introduced in Eq. 30 is

$$\mathbf{D}=\begin{pmatrix}d_{11}&d_{12}&d_{13}\\d_{21}&d_{22}&d_{23}\\0&0&0\end{pmatrix} \tag{44}$$

where

$$\begin{aligned}
d_{11} &= \frac{-y_{\mathrm{p}0}}{(1-\nu+x_{\mathrm{g}0}-x_{\mathrm{p}0})^2+y_{\mathrm{p}0}^2},\quad d_{12}=-d_{11},\\
d_{13} &= \frac{1-\nu+x_{\mathrm{g}0}-x_{\mathrm{p}0}}{(1-\nu+x_{\mathrm{g}0}-x_{\mathrm{p}0})^2+y_{\mathrm{p}0}^2},\\
d_{21} &= \frac{-(1-\nu+x_{\mathrm{g}0}-x_{\mathrm{p}0})^3-(-\nu+x_{\mathrm{g}0}-x_{\mathrm{p}0})y_{\mathrm{p}0}^2}{\left((1-\nu+x_{\mathrm{g}0}-x_{\mathrm{p}0})^2+y_{\mathrm{p}0}^2\right)^{\frac{3}{2}}},\quad d_{22}=-d_{21},\\
d_{23} &= -y_{\mathrm{p}0}\frac{(\nu-1)(\nu-2)+(x_{\mathrm{p}0}-x_{\mathrm{g}0})^2+y_{\mathrm{p}0}^2+(2\nu-3)(x_{\mathrm{p}0}-x_{\mathrm{g}0})}{\left((1-\nu+x_{\mathrm{g}0}-x_{\mathrm{p}0})^2+y_{\mathrm{p}0}^2\right)^{\frac{3}{2}}}.
\end{aligned} \tag{45}$$

$\mathbf{D}_{\mathrm{w}}$ is

$$D_{\mathrm{w}}=\begin{pmatrix}0&0&0\\w_{21}&w_{22}&w_{23}\\0&0&0\end{pmatrix}, \tag{46}$$

where

$$\begin{aligned}
w_{21} &= \frac{(1-\nu+x_{\mathrm{g}0}-x_{\mathrm{p}0})^3+(x_{\mathrm{g}0}-x_{\mathrm{p}0})y_{\mathrm{p}0}^2}{\left((1-\nu+x_{\mathrm{g}0}-x_{\mathrm{p}0})^2+y_{\mathrm{p}0}^2\right)^{\frac{3}{2}}},\quad w_{22}=-w_{21},\\
w_{23} &= \frac{(1-\nu+x_{\mathrm{g}0}-x_{\mathrm{p}0})(2-2\nu+x_{\mathrm{g}0}-x_{\mathrm{p}0})y_{\mathrm{p}0}+y_{\mathrm{p}0}^3}{\left((1-\nu+x_{\mathrm{g}0}-x_{\mathrm{p}0})^2+y_{\mathrm{p}0}^2\right)^{\frac{3}{2}}}.
\end{aligned} \tag{47}$$

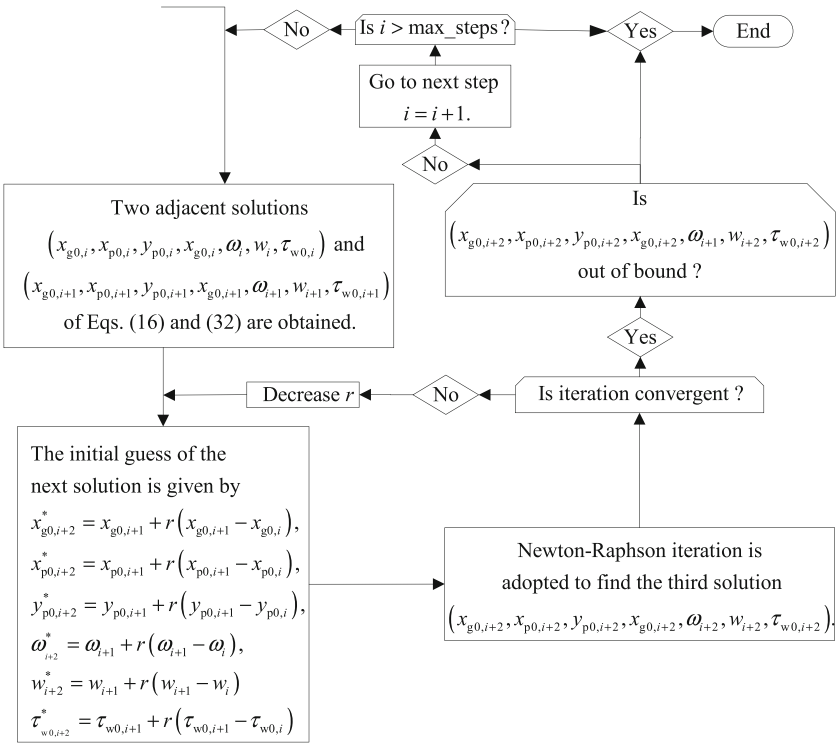

Fig. 20 Continuation scheme with eigenvalue calculation for the stability boundaries

$\mathbf{D}_g$ is

$$\mathbf{D}_g = \begin{pmatrix} 0 & 0 & 0 \\ g_{21} & g_{22} & g_{23} \\ 0 & 0 & 0 \end{pmatrix}, \tag{48}$$

where

$$g_{21} = gw_{21}, \quad g_{22} = gw_{22}, \quad g_{23} = gw_{23}. \tag{49}$$

$\mathbf{D}_v$ is

$$\mathbf{D}_v = \begin{pmatrix} 0 & 0 & 0 \\ 0 & 0 & 0 \\ v_{31} & v_{32} & v_{33} \end{pmatrix}, \tag{50}$$

where

$$v_{31} = d_{11}, \quad v_{32} = d_{12}, \quad v_{33}d_{13}. \tag{51}$$

Appendix C Continuation

A block diagram of the continuation algorithm employed for stability analysis is illustrated in Fig. 20. As seen, the algorithm is an iterative *trial-and-correct* procedure. The scheme is started with two known adjacent solutions (the ith and the $i + 1$st solutions), and the guess for the third (the $i + 2$nd) is given with a relaxation parameter r. Next, the Newton-Raphson iteration scheme is adopted to correct the guess. In case of non-convergence iteration, r is decreased for a new guess, until the iteration converges for the third solution. Moreover, the new solution is accepted only if it is located in the predefined region. Next, the algorithm goes to next loop ($i = i + 1$) if the solutions are insufficient $i <$ max_steps.

References

1. Altintas Y, Weck M (2004) Chatter stability of metal cutting and grinding. CIRP Ann - Manuf Technol 53(2):619–642. doi:10.1016/S0007-8506(07)60032-8
2. Arnold RN (1946) The mechanism of tool vibration in the cutting of steel. In: Proceedings of the Institution of Mechanical Engineers, vol 154, London, pp 261–284
3. Badger J, Murphy S, O'Donnell G (2011) The effect of wheel eccentricity and run-out on grinding forces, waviness, wheel wear and chatter. Int J Mach Tools Manuf 51(10–11):766–774. doi:10.1016/j.ijmachtools.2011.06.006. 2011/11//
4. Chatterjee S (2011) Self-excited oscillation under nonlinear feedback with time-delay. J Sound Vibr 330(9):1860–1876. doi:10.1016/j.jsv.2010.11.005
5. Chung K. W, Liu Z (2011) Nonlinear analysis of chatter vibration in a cylindrical transverse grinding process with two time delays using a nonlinear time transformation method. Nonlinear Dyn 66:441–456. doi:10.1007/s11071-010-9924-y
6. Dassanayake AV, Suh CS (2007) Machining dynamics involving whirling part i: model development and validation. J Vibr Control 13(5):475 –506. doi:10.1177/1077546307074230
7. Dassanayake AV, Suh CS (2007) Machining dynamics involving whirling part ii: machining motions described by nonlinear and linearized models. J Vibr Control 13(5):507 –526. doi:10.1177./1077546307074238
8. Diken H (2001) Non-linear vibration analysis and subharmonic whirl frequencies of the jeffcott rotor model. J Sound Vibr 243(1):117–125. doi:10.1006/jsvi.2000.3394
9. Durgumahanti USP, Singh V, Rao PV (2010) A new model for grinding force prediction and analysis. Int J Mach Tools Manuf 50(3):231–240. doi:10.1016/j.ijmachtools.2009.12.004
10. Hahn RS (1954) Worcester, Mass: on the theory of regenerative chatter in precision-grinding operations. Trans ASME 76(1): 593–597
11. Huang J, Luo ACJ (2015) Analytical solutions of period-1 motions in a buckled, nonlinear jeffcott rotor system. Int J Dyn Control:1–8. doi:10.1007/s40435-015-0149-2
12. Huang J, Luo ACJ (2015) Periodic motions and bifurcation trees in a buckled, nonlinear jeffcott rotor system. Int J Bifurcation Chaos 25(01):1550,002. doi:10.1142/S0218127415500029
13. Huang P, Lee WB, Chan CY (2015) Investigation of the effects of spindle unbalance induced error motion on machining accuracy in ultra-precision diamond turning. Int J Mach Tools Manuf 94:48–56. doi:10.1016/j.ijmachtools.2015.04.007
14. Inasaki I, Karpuschewski B, Lee H. S Grinding chatter0—origin and suppression. CIRP Ann - Manuf Technol 2(50):515–534. doi:10.1016/S0007-8506(07)62992-8
15. Inazaki I, Yonetsu S (1969) Forced vibrations during surface grinding. Bull JSME 12(50):385–391
16. Jeffcott H. H (1919) The lateral vibration of loaded shafts in the neighbourhood of a whirling speed.—the effect of want of balance. Philos Mag Series 6 37(219):304–314. doi:10.1080/14786440308635889
17. Karpenko E. V, Pavlovskaia E. E, Wiercigroch M (2003) Bifurcation analysis of a preloaded jeffcott rotor. Chaos, Solitons Fractals 15(2):407–416. doi:10.1016/S0960-0779(02)00107-8
18. Karpenko E. V, Wiercigroch M, Pavlovskaia E. E, Cartmell M. P (2002) Piecewise approximate analytical solutions for a jeffcott rotor with a snubber ring. Int J Mech Sci 44(3):475–488. doi:10.1016/S0020-7403(01)00108-4
19. Kim P, Jung J, Lee S, Seok J (2013) Stability and bifurcation analyses of chatter vibrations in a nonlinear cylindrical traverse grinding process. J Sound Vibr 332(15):3879 – 3896. doi:10.1016/j.jsv.2013.02.009
20. Kuznetsov YA (2000) Elements of applied bifurcation theory
21. Li H, Shin YC (2007) A study on chatter boundaries of cylindrical plunge grinding with process condition-dependent dynamics. Int J Mach Tools Manuf 47:1563–1572
22. Lichun L, Jizai F, Peklenik J (1980) A study of grinding force mathematical model. CIRP Ann - Manuf Technol 29(1):245–249. doi:10.1016/S0007-8506(07)61330-4
23. Liu X, Vlajic N, Long X, Meng G, Balachandran B (2013) Nonlinear motions of a flexible rotor with a drill bit: stick-slip and delay effects. Nonlinear Dyn 72(1-2):61–77. doi:10.1007/s11071-012-0690-x
24. Liu ZH, Payre G (2007) Stability analysis of doubly regenerative cylindrical grinding process. J Sound Vibr 301(2):950–962. doi:10.1016/j.jsv.2006.10.041
25. Long XH, Balachandran B (2007) Stability analysis for milling process. Nonlinear Dyn 49(3):349–359. doi:10.1007/s11071-006-9127-8
26. Malkin S, Guo C (2007) Grinding technology. Industrial Press Inc., USA
27. Molnár TG, Insperger T, Hogan SJ, Stépán G (2016) Estimation of the bistable zone for machining operations for the case of a

distributed cutting force model. ASME J Comput Nonlinear Dyn 11:051,008. doi:10.1115/1.4032443
28. Nayfeh AH (2008) Order reduction of retarded nonlinear systems—the method of multiple cales versus center-manifold reduction. Nonlinear Dyn 51:483–500. doi:10.1007/s11071-007-9237-y
29. Nayfeh AH, Balachandran B (2004) Applied nonlinear dynamics: analytical, computational, and experimental methods. WILEY-VCH Verlag GmbH & Co. KGaA, Weinheim
30. Páez Chávez J, Wiercigroch M (2013) Bifurcation analysis of periodic orbits of a non-smooth jeffcott rotor model. Commun Nonlinear Sci Numer Simul 18(9):2571–2580. doi:10.1016/j.cnsns.2012.12.007
31. Páez Chávez J, Vaziri Hamaneh V, Wiercigroch M (2015) Modelling and experimental verification of an asymmetric jeffcott rotor with radial clearance. J Sound Vibr 334:86–97. doi:10.1016/j.jsv.2014.05.049
32. Rafieian F, Girardin F, Liu Z, Thomas M, Hazel B (2014) Angular analysis of the cyclic impacting oscillations in a robotic grinding process. Mech Syst Signal Process 44(1–2):160–176. doi:10.1016/j.ymssp.2013.05.005
33. Rao J. S (2001) A note on jeffcott warped rotor. Mech Mach Theory 36(5):563–575. doi:10.1016/S0094-114X(01)00008-8
34. Rowe WB (2009) Principles of modern grinding techonology. William Andrew, Burlington, MA
35. Snoeys R (1969) Dominating parameters in grinding wheel and workpiece regenerative chatter. In: Proceeding of The 10th International Conference on Machine Tool Design and Research. University of Birmingham, pp 325–348
36. Tauhiduzzaman M, Yip A, Veldhuis SC (2015) Form error in diamond turning. Precis Eng 42:22–36. doi:10.1016/j.precisioneng.2015.03.006
37. Thompson RA (1974) On the doubly regenerative stability of a grinder. ASME J Eng Ind 96(1):275–280. doi:10.1115/1.3438310
38. Thompson R. A (1977) On the doubly regenerative stability of a grinder: the combined effect of wheel and workpiece speed. ASME J Eng Ind 99(1):237–241. doi:10.1115/1.3439144
39. Thompson RA (1986) On the doubly regenerative stability of a grinder: the mathematica analysis of chatter growth. ASME J Eng Ind 108(2):83–92. doi:10.1115/1.3187055
40. Thompson R. A (1986) On the doubly regenerative stability of a grinder: the theory of chatter growth. ASME J Eng Ind 108(2):75–82. doi:10.1115/1.3187054
41. Thompson R. A (1992) On the doubly regenerative stability of a grinder: the effect of contact stiffness and wave filtering. ASME J Eng Ind 114(1):53–60. doi:10.1115/1.2899758
42. Vlajic N, Liu X, Karki H, Balachandran B (2014) Torsional oscillations of a rotor with continuous stator contact. Int J Mech Sci 83:65–75. doi:10.1016/j.ijmecsci.2014.03.025
43. Wiercigroch M, Budak E (2001) Sources of nonlinearities, chatter generation and suppression in metal cutting. Philos Trans Royal Soc London. Ser A: Math, Phys Eng Sci 359(1781):663–693. doi:10.1098/rsta.2000.0750
44. Yan Y, Xu J (2013) Suppression of regenerative chatter in a plunge-grinding process by spindle speed. ASME J Manuf Sci Eng 135(4):041,019–041,019. doi:10.1115/1.4023724
45. Yan Y, Xu J, Wang W (2012) Nonlinear chatter with large amplitude in a cylindrical plunge grinding process. Nonlinear Dyn 69(4):1781–1793. doi:10.1007/s11071-012-0385-3
46. Yan Y, Xu J, Wiercigroch M (2014) Chatter in a transverse grinding process. J Sound Vibr 333(3):937–953. doi:10.1016/j.jsv.2013.09.039
47. Yan Y, Xu J, Wiercigroch M (2015) Non-linear analysis and quench control of chatter in plunge grinding. Int J Non-Linear Mech 70:134–144. doi:10.1016/j.ijnonlinmec.2014.06.012
48. Yuan L, Keskinen E, Jarvenpaa VM (2005) Stability analysis of roll grinding system with double time delay effects. In: Ulbrich H, Gunthner W (eds) Proceedings of IUTAM Symposium on Vibration Control of Nonlinear Mechanisms and Structures, vol 130. Springer, Netherlands, pp 375–387
49. Zhai L, Luo Y, Wang Z, Kitauchi S, Miyagawa K (2016) Nonlinear vibration induced by the water-film whirl and whip in a sliding bearing rotor system. Chin J Mech Eng 29(2):260–270. doi:10.3901/CJME.2015.0713.092